Exp Fluids (2016) 57:55
DOI 10.1007/s00348-016-2144-6

RESEARCH ARTICLE

Study of bubble-induced turbulence in upward laminar bubbly pipe flows measured with a two-phase particle image velocimetry

Minki Kim[1] · Jun Ho Lee[1] · Hyungmin Park[1,2]

Received: 28 September 2015 / Revised: 7 January 2016 / Accepted: 18 February 2016 / Published online: 30 March 2016

Abstract In the present study, focusing on characterizing the bubble-induced agitation (turbulence), spatially varying flow statistics of gas and liquid phases in laminar upward bubbly flows (Reynolds number of 750) with varying mean void fraction are investigated using a two-phase high-speed particle image velocimetry. As the flow develops along the vertical direction, bubbles with small-to-moderate void fractions, which were intentionally distributed asymmetrically at the inlet, migrate fast and show symmetric distributions of wall or intermediate peaking. Meanwhile, the mean liquid velocity saturates relatively slowly to a flat distribution at the core region. Despite small void fractions considered, the bubbles generate a substantial turbulence, which increases with increasing mean void fraction. Interestingly, it is found that the mean vertical velocity, bubble-induced normal stress in radial direction, and Reynolds stress profiles match well with those of a single-phase turbulent flow at a moderate Reynolds number (e.g., 10^4), indicating the similarity between the bubble-induced turbulence and wall-shear-generated turbulence in a single-phase flow. Previously suggested scaling relations are confirmed such that the mean bubble rise velocity and bubble-induced normal stress (in both vertical and radial directions) scale with mean volume void fraction as a power of −0.1 and 0.4, respectively. Finally, based on the analysis of measured bubble dynamics (rise in an oscillating path), a theoretical model for two-phase turbulent (Reynolds) stress is proposed, which includes the contributions by the non-uniform distributions of local void fraction and relative bubble rise velocity, and is further validated with the present experimental data to show a good agreement with each other.

1 Introduction

In studying gas–liquid flows, the modulation of liquid-phase turbulence due to gas phase is an important issue, because it predominantly determines the thermal-fluid characteristics such as heat transfer, pressure drop, and mixing that have critical influences on the performance and safety of various systems in power generation and conversion, wastewater treatment, oil extraction, mineral processing, and nuclear reactors. As a specific type of gas–liquid flows, bubbly flow is an attractive option for the industrial applications because of the large-scale mixing rates that can be achieved without moving mechanical parts, even at relatively small Reynolds numbers. Thus, many researches have been performed to understand the turbulence modification in bubbly pipe (channel) flows. Although some issues still remain to be solved, previous efforts have shown that bubbles enhance or suppress the liquid-phase turbulence, depending on bubble size, void distribution, ratio of liquid to gas fluxes, bubble deformability, and the localized effects at the core and wall regions (Serizawa et al. 1975; Theofanous and Sullivan 1982; Wang et al. 1987; Lance and Bataille 1991; Liu and Bankoff 1993; So et al. 2002; Hosokawa and Tomiyama 2004, 2013; Shawkat et al. 2008). For example, it has been shown that for a given liquid flux, the liquid-phase turbulence is enhanced (at both

Electronic supplementary material The online version of this article (doi:10.1007/s00348-016-2144-6) contains supplementary material, which is available to authorized users.

✉ Hyungmin Park
hminpark@snu.ac.kr

[1] Department of Mechanical & Aerospace Engineering, Seoul National University, Seoul 08826, Korea

[2] Institute of Advanced Machines and Design, Seoul National University, Seoul 08826, Korea

the core and the wall regions) with a comparatively larger gas flux, but is suppressed by a relatively smaller gas flux (Serizawa et al. 1975; Wang et al. 1987; Liu and Bankoff 1993; Shawkat et al. 2008). Interestingly, the suppression of a liquid-phase turbulence occurs locally different, e.g., at the core (Liu and Bankoff 1993), wall region (Shawkat et al. 2008), or both regions (So et al. 2002). In addition, the turbulence modification has a dependency on the bubble size. Gore and Crowe (1989) suggested that the liquid-phase turbulence is enhanced (suppressed) when the ratio of bubble size to the integral length scale of the liquid-phase flow is approximately larger (smaller) than 0.1. Fujiwara et al. (2004) also measured the turbulence suppression with small-sized bubbles.

As introduced briefly above, the trend of turbulence modulation in the two-phase flows appears to be very complex, being affected by various parameters of liquid and gas phases. Thus, the interests of many researches have moved to understand the nature of two-phase flow turbulence. It is roughly accepted that the two-phase flow turbulence has two contributions: one from the shear-induced turbulence (SIT) that already exists in a single-phase flow and the other from the bubble-induced turbulence (BIT) (Theofanous and Sullivan 1982; Michiyoshi and Serizawa 1986; Lance and Bataille 1991; Martínez-Mercado et al. 2007; Riboux et al. 2010, 2013; Hosokawa and Tomiyama 2013). Theofanous and Sullivan (1982) commented that the effects of bubble agitation occur as an additive to the wall-shear-generated turbulence. Similarly, Liu and Bankoff (1993) estimated the ratio of bubble-induced turbulence energy to total turbulence, assuming that the two-phase flow turbulence is a sum of SIT and BIT. As Lance and Bataille (1991) pointed out the importance of distinguishing the pure liquid agitation due to bubbles (the so-called pseudo-turbulence) and the bubble-induced modulation of the intrinsic SIT, however, this simple superposition has a limitation to be applied to gas–liquid flows with wide range of different conditions (Wang et al. 1987; Liu and Bankoff 1993).

Since the role of bubble-induced agitation in two-phase bubbly flows shows up in a complex manner depending on the examined conditions, before investigating the two-way coupling between SIT and BIT, we think that it is necessary to first understand the pure bubble-induced agitation, as commented by Riboux et al. (2010). In this context, a laminar flow is a good condition (as a reasonable limiting case) to study the nature of bubble-induced agitation (Kashinsky et al. 1993; Hosokawa and Tomiyama 2013). Previously, Antal et al. (1991) and Azitarte and Buscaglia (2003) simulated upward laminar bubbly flows to validate their two-fluid model in terms of void distribution and mean liquid velocity. Biswas et al. (2005) and Lu et al. (2006) performed a direct numerical simulation and showed that the turbulence profile has a peak near the wall, accompanied with the wall-peaking void distribution. Although Kashinsky et al. (1993) have measured the liquid velocity fluctuation together with void distribution, a few existing experimental studies such as Song et al. (2001) and Luo et al. (2003) only have provided the limited information about the gas-phase-like void distribution and bubble size. In overall, these prior studies have not provided a detailed analysis of the liquid-phase flow modification (turbulence characteristics, in particular) in a close relationship to the gas-phase condition. Recently, Hosokawa and Tomiyama (2013) performed a detailed LDV measurement to investigate the relation between the turbulence statistics (turbulence intensity, Reynolds stress, and turbulent kinetic energy) and the void condition in a vertical pipe flow at $Re_D = u_b D/\nu = 900$ (u_b liquid bulk velocity, D pipe diameter, and ν liquid kinematic viscosity), while varying mean void fraction. They showed the validation of Kolmogorov's $-5/3$ law (same as that in a single-phase turbulent flow) in a two-phase flow and also proposed a two-phase turbulent stress model.

To study the nature of bubble-induced agitation in more detail, on the other hand, it is highly required to measure the temporal and spatial variations of gas and liquid phases together. In particular, it would be meaningful to measure (i.e., visualize) the instantaneous flow structure (bubble wake, in particular) to deepen our understanding of the two-phase interaction represented as a profile of time-averaged flow statistics on which most previous studies have focused so far. Furthermore, the origin of bubble-induced turbulence has been attributed to the dynamics of near-wake behind the bubbles (Lance and Bataille 1991; Rensen et al. 2005; Riboux et al. 2010, 2013). Thus an optical measurement technique like two-phase particle image velocimetry method is considered to be suitable to achieve the above requirement. Previously, several studies have demonstrated the capability of two-phase PIV method to measure the gas and liquid phases simultaneously (Lindken and Merzkirch 2002; Bröder and Sommerfeld 2007; Sathe et al. 2010); however, there are a few studies that fully utilized a two-phase PIV (i.e., simultaneous measurement of gas and liquid phases) to investigate the bubble-induced turbulence (Fujiwara et al. 2004; Liu et al. 2005; Pang and Wei 2013).

In summary, despite previous intensive efforts, we think that (i) the temporal and spatial changes (i.e., visualization) in instantaneous flow fields and (ii) the detailed relation between the bubble dynamics and liquid flow statistics are still needed to be investigated more in laminar bubbly flows. Therefore, we experimentally investigate the gas–liquid flow statistics in upward laminar bubbly pipe flows using a two-phase particle image velocimetry (PIV/LIF with shadowgraph) method. As pointed out in a recent review by Tryggvason and Lu (2015), most previous

studies on bubbly flows tended to focus on the statistically steady state (i.e., fully developed stage), though the evolving (transient) process is more complex and as important as the steady state. Therefore, to understand the evolution of flow, we introduce asymmetrically distributed bubbles at the inlet and measure the flows at three streamwise locations including developing and fully developed regions. Here, we are mainly interested in (i) explaining the nature of bubble-induced agitation (turbulence) in relation to the void condition and bubble dynamics, (ii) discussing the similarity between the pure bubble-induced turbulence and the single-phase flow turbulence, (iii) suggesting a theoretical model to predict the two-phase flow turbulence, and (iv) providing detailed experimental data for gas and liquid phases in laminar bubbly flows.

2 Experimental setup and procedures

2.1 Upward laminar bubbly pipe flow

The experiments are carried out in a circulating loop system that includes a vertical pipe (inner diameter, D of 40 mm), water pump, air compressor, upper tank, reservoir, and bubble-generating mechanism (Fig. 1a). From the reservoir, water at room temperature is supplied by a water pump (PM-403PI, WILO pump Ltd.) into a vertically aligned circular pipe in upward direction. To regulate the flow precisely, the waterline is divided into two ways and monitored with separate flow meters with one (KTM-800, KOMETER) for high (0.08–11.304 $m^3\ h^{-1}$) and the other (KIR-570-F-1, KOMETER) for low (0.015–0.48 $m^3\ h^{-1}$) flow rates, respectively. The test section is a 1730-mm-high (about 42D) pipe made of an acrylic and wrapped by a transparent acrylic rectangular jacket (width of 90 mm). The space between the circular pipe and jacket is filled with water to reduce the distortion in the optical images due to the curved wall and the different refractive indices of water and acrylic.

The air, generated by the air compressor and purified by a filter, is introduced to the bubble-generating mechanism in which the pressure is controlled through a regulator. The bubble-generating mechanism, located before the pipe inlet, is designed based on a previous study by Hosokawa and Tomiyama (2013) to create air bubbles with an almost constant size through a mixing process. As shown in Fig. 1b, the airflows fed through four holes distributed circumferentially are mixed with water supplied through the sub-passage and then spread into the main water passage via 1-mm-gap slit. Thus, by controlling the flow rate of sub-water passage, i.e., the shear of water flow near the air injection holes, the bubble size can be controlled (Hosokawa and Tomiyama 2013). The airflow rate is regulated by solenoid valves located at the inlet of the bubble-generating mechanism. Each solenoid valve per a conduit for air passage is controlled separately via a timing hub (MotionPro XS-TH, IDT Inc.) at the frequency of 20 Hz (with a duration of 13 ms for opening), which has been optimized to produce the bubbly flows with a more or less uniformly distributed bubble size (see

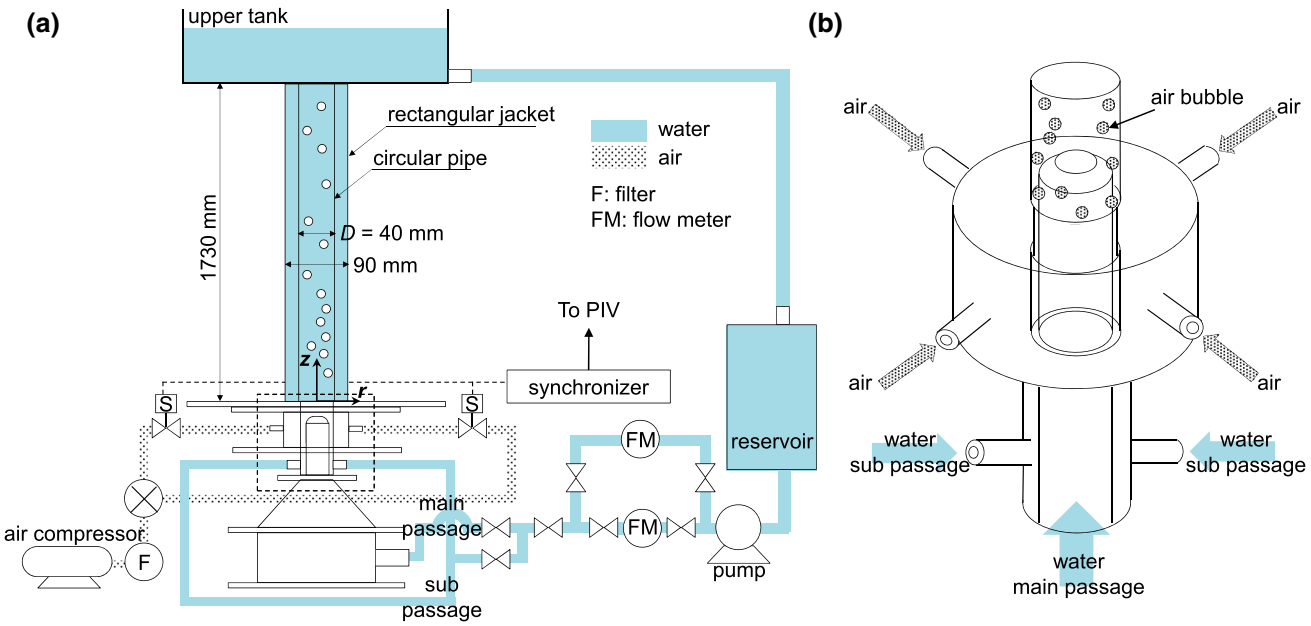

Fig. 1 **a** Schematic diagram for the experimental setup to generate upward bubbly pipe flows. **b** Details of the bubble generation mechanism that is highlighted as a *dashed box* in (**a**), adopted from Hosokawa and Tomiyama (2013)

Fig. 4) but minimizing the events of bubble coalescence or breakup.

2.2 Two-phase particle image velocimetry

The major requirement of two-phase particle image velocimetry to measure gas–liquid flows is reliable phase discrimination, and to achieve this, several different arrangements of cameras and illuminations have been employed so far (Sathe et al. 2010). In the present study, as shown in Fig. 2, we consider the method of PIV/LIF with shadowgraph that consists of one camera and two illuminations (Lindken and Merzkirch 2002; Bröder and Sommerfeld 2007). That is, a single high-speed camera (SpeedSense M310, Dantec Dynamics) captures the images of both gas and liquid phases (at 270 Hz with a resolution of 1280 × 800 pixels), while the phase separation is further achieved by processing the acquired digital images that were illuminated by two sources with different wavelengths. For gas phase, an in-house LED array (red-colored, wavelength of 675 nm) is used to produce the shadow images of bubbles while a green laser sheet (wavelength of 532 nm) from a continuous-wave (CW) laser (RayPower 5000, Dantec Dynamics) illuminates the fluorescent seeding particles (PMMA-Rhodamine B). The fluorescent tracking particles are used to reduce the interference caused by laser light reflection. Also, a mirror is placed at the opposite side of CW laser to minimize the blocking of laser sheet by rising bubbles. Here, it is important to confirm to have a planar illumination after the laser sheet is reflected by the mirror, avoiding a volumetric illumination. To achieve this, the position and incidence angle of the mirror were made to be controlled, by which the optimal orientation of the mirror is found such that the original and reflected laser sheets illuminate the same vertical line that is marked on the in-house calibration target used to calibrate the spatial resolution of two-phase PIV. Assisted by the difference in the wavelength of two illuminations, the camera equipped with an orange filter (high-pass cutoff wavelength of ∼520 nm) finally obtains the images of bubble shadows and seeding particles of which the grayscale levels are different from each other (different from the background as well). An example of raw image that has been captured with the present setup is shown in Fig. 3a.

After the raw images are obtained, they are separated into two (details are explained in Sect. 2.3): The one for seeding particles is evaluated to measure the liquid velocity and the other for bubble shadows is processed to calculate the gas-phase statistics. The images of tracking particles are evaluated by cross-correlation using fast Fourier transform algorithm (interrogation window of 32 × 32 pixels and 75 % overlap). When the outliers whose size is larger than three times the standard deviation of the size of mean velocity vector are detected, they are replaced by vectors that are interpolated from the surrounding velocity vectors in 3 × 3 grids. From the images of bubble shadows, the velocity is determined by calculating the translation of the bubble centroid, and typical particle tracking velocimetry (PTV) algorithm is used to track each bubble. To avoid matching wrong bubbles, the condition of thresholding the

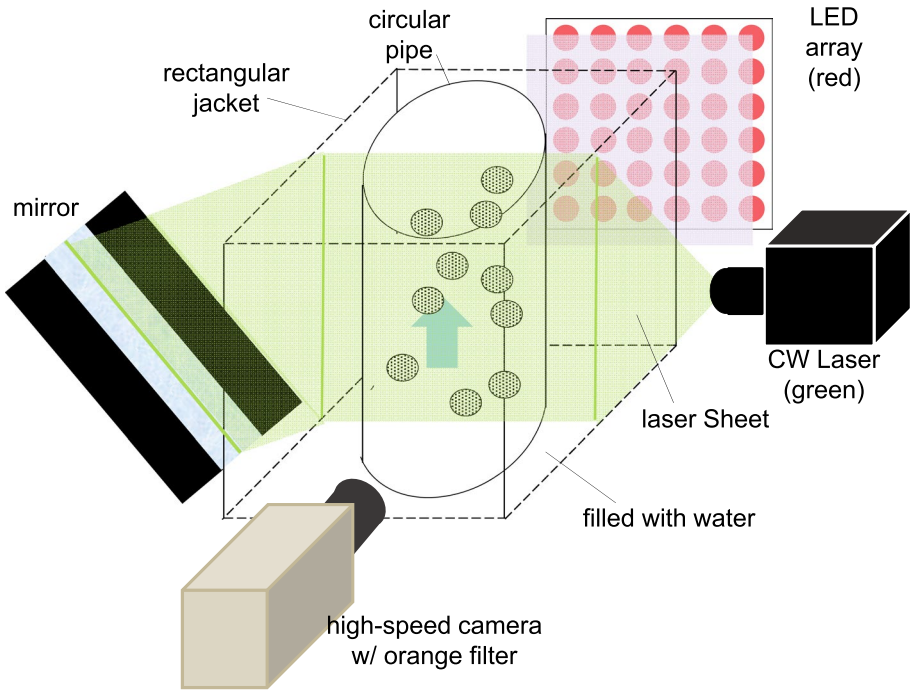

Fig. 2 Experimental setup for two-phase particle image velocimetry measurement

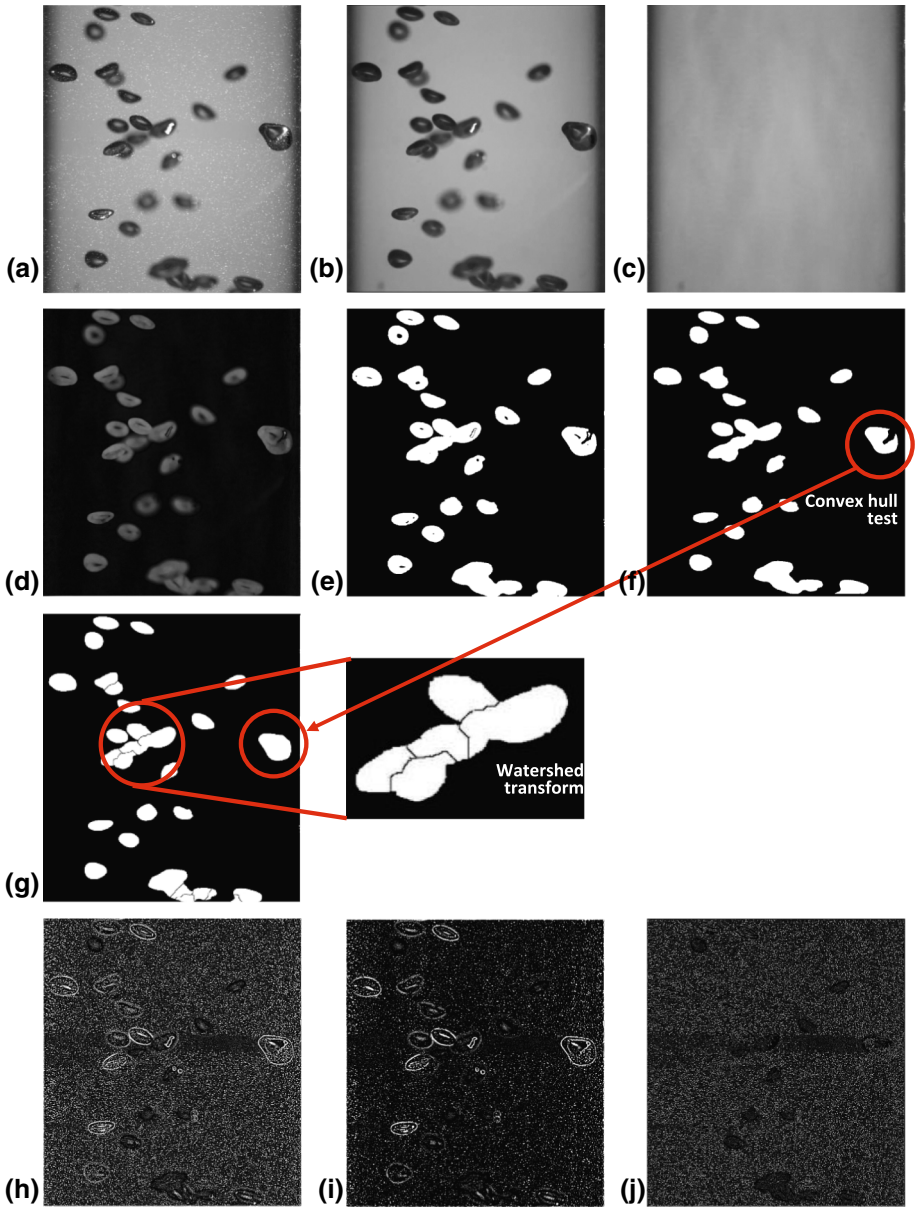

Fig. 3 Example images for phase separation from a raw image **a** to gas (g) and liquid (**j**) phases, corresponding to the outcomes from each process step in Fig. S2 (see supplementary material)

maximum bubble velocity and its change are applied (Baek and Lee 1996). The centroid of each bubble is found by calculating the area center of two-dimensional bubble shadow image. Further discussions are provided in Sect. 2.4 for estimating the bubble shape based on two-dimensional shadow image.

The actual measurements are performed at three streamwise locations (on the center plane) at $z/D = 4.5$, 21, and 42, of which the first two and last locations belong to the developing and fully developed regions, respectively. Considered Reynolds number for the single-phase laminar flow is $Re_D = 750$, based on the bulk velocity (u_b). According to Kays and Crawford (1993), the entrance length (L_e) in a laminar pipe flow is given by $L_e \simeq 0.05 Re_D$, which is estimated about $37.5D$ for the present study and the single-phase mean streamwise velocity profiles measured at each location validate this (see Fig. S1 in the supplementary material).

As noted, the present measurements provide two-dimensional flow fields on the center plane and thus the entire three-dimensional flow structures may not be fully examined. However, we consider void fractions that are not large enough to induce a vigorous bubble coalescence, the background turbulence is not strong enough to cause a bubble breakup frequently, and the flow in the radial direction (i.e., out-of-plane motion) in the background (laminar) flow is also negligible. Thus, we think that the present measurement provides us useful information about the bubble-induced turbulence in laminar flows. Furthermore, in the literature, it is possible to find that many prior studies

have investigated the bubbly flows (even in a turbulent flow regime) in vertical pipe (Lindken and Merzkirch 2002; Fujiwara et al. 2004; Bröder and Sommerfeld 2007; Zhou et al. 2013) and channel (Delnoij et al. 2000; So et al. 2002; Sathe et al. 2010; Pang and Wei 2013) flows, based on the measurement (using a similar particle image velocimetry or laser Doppler velocimetry) on a two-dimensional plane.

2.3 Image processing

We achieve the phase discrimination in the raw image using the fact that the grayscale levels corresponding to bubble shadow, seeding particles, and background are different. Figure 3 shows the example images corresponding to each step in our image precessing method (for the process chart, see Fig. S2 in the supplementary material). The first step is a removal of the images of tracking particles from a raw image (Fig. 3a) by applying a mean filter (7 × 7 pixels) to the raw image (Fig. 3b). In the meanwhile, a background image without bubbles but with water filling the test section is acquired separately (Fig. 3c), which is extracted from the raw image, and the result is shown in Fig. 3d. Then, it is binarized with a threshold determined by an optimal global thresholding algorithm of Otsu (1979), which finds the optimal threshold that maximizes the between-class variance from a grayscale histogram of the image. Since the bubble image is brighter than the background, there are two peaks in the grayscale histogram and thus the optimal threshold value can be easily found (Fig. 3d). As shown in Fig. 3e, a simple binarization is not enough to capture the bubble shape accurately and additional treatments are necessary. That is, the opening of the binarized image with a structuring element of 5 × 5 matrix suppresses bright noises smaller than the structuring element and makes the bubble interface smoother (Gonzalez et al. 2011). Also, by applying a size filter, intensive residuals caused by the reflection on bubble interface are eliminated (Lindken and Merzkirch 2002; Zhou et al. 2013) and holes inside bubbles caused by the large curvature of a bubble interface are filled up (Lindken and Merzkirch 2002; Sathe et al. 2010). Finally, to correct the size of binarized bubble that tends to be overestimated, a border of 3 pixels of each bubble is eliminated, which results in the reconstructed bubble shadow images (Fig. 3f).

Next step is to identify each bubble while sorting out overlapped ones. We use a watershed segmentation algorithm to distinguish individual bubble in the areas occupied commonly by multiple bubbles (Lau et al. 2013). As shown in Fig. 3a, bubble image has a bright inner part and thus the watershed transform can be employed to find the catchment basins (brighter parts) and watershed ridge lines (darker parts) in the mean-filtered image (Fig. 3b). Before applying the watershed algorithm, a convex hull test is performed to (i) smoothen the rough boundary of bubble, (ii) fill the lost parts of bubble caused by reflection of a laser sheet at bubble surface, and (iii) prevent non-overlapped bubbles from being divided. A convex hull is defined as the smallest convex polygon that can contain the specified region. Thus, the portion of bubble image divided by the convex area is a criterion to determine whether the bubble has to be processed further by watershed segmentation (for overlapped bubbles) or all pixels within the hull should be filled in (for solitary bubbles). After the images in Fig. 3f are processed further, finally the position and shape of each bubble are identified in Fig. 3g from which gas-phase statistics are evaluated. The bubble images in Fig. 3g include both in-focused and out-of-focused ones, and it is necessary to distinguish them. Using the fact that the out-of-focused bubbles have a small gradient in the grayscale level at bubble interface, a Sobel (gradient enhancement) filter (3 × 3 pixels) is applied to detect the edge of in-focused bubbles (Bröder and Sommerfeld 2007; Pang and Wei 2013) and they are tagged digitally to be distinguished from out-of-focused bubbles.

For the separation of liquid phase (Bröder and Sommerfeld 2007; Pang and Wei 2013), we first apply Laplacian of Gaussian (LoG) filter to the raw image in order to detect the edges of both bubbles and seeding particles (Fig. 3h). Then, a median filter is applied to the LoG-filtered image to identify the boundaries of bubbles (Fig. 3i). Finally, the image for liquid phase (i.e., image of tracking particles only) is obtained by subtracting the bubble contour image from LoG-filtered image (Fig. 3j).

2.4 Conditions of gas phase

In order to investigate the flow evolution along the streamwise direction, we intentionally introduce asymmetrically distributed bubbles at the inlet, by using two of four conduits for air passages (Fig. 1b). The mean volume void fraction is varied as $\langle\bar{\alpha}\rangle = 0.05$, 0.10, 0.17, and 0.64 % (see Table 1 for the details), which is the averaged ratio of volume occupied by bubbles to the volume of test section. On the other hand, the size of bubble is characterized from the bubble shadow image projected on a two-dimensional plane. As classified by Reynolds and Eötvös numbers (Clift et al. 1978), the bubbles in the present study have a wobbling shape (see Figs. 5, 6) that has been approximated as an oblate ellipsoid in previous studies (Fujiwara et al. 2004; Jeong and Park 2015). Therefore, based on the projected shape on the two-dimensional plane, the equivalent bubble diameter (d_e) is calculated as $d_e = (d_h^2 d_v)^{1/3}$, where d_h and d_v are the lengths of horizontal (major) and vertical (minor) axes of an oblate ellipsoidal bubble, respectively.

Table 1 Conditions for the considered gas phase

Case	j_L (ms^{-1})	j_G (ms^{-1})	$\langle\bar{\alpha}\rangle$ (%)	$\langle\bar{d}_e\rangle$ (mm)	Re_b	We	Eo	Mo
1	1.88×10^{-2}	3.95×10^{-3}	0.05	2.2 (0.74)	600	2.0	0.65	2.54×10^{-11}
2	1.88×10^{-2}	6.05×10^{-3}	0.10	2.7 (0.85)	680	2.3	0.98	2.54×10^{-11}
3	1.88×10^{-2}	8.41×10^{-3}	0.17	3.1 (1.09)	740	2.6	1.29	2.54×10^{-11}
4	1.88×10^{-2}	2.44×10^{-2}	0.64	3.7 (1.51)	880	2.9	1.83	2.54×10^{-11}

j_L liquid flux, j_G gas flux, $\langle\bar{d}_e\rangle$ equivalent bubble diameter, $Re_b = v_r\langle\bar{d}_e\rangle\nu^{-1}$ bubble Reynolds number based on the relative rise velocity (v_r), $We = \rho_l v_r^2\langle\bar{d}_e\rangle\sigma^{-1}$ Weber number, $Eo = g(\rho_l - \rho_g)\langle\bar{d}_e\rangle^2\sigma^{-1}$ Eötvös number, $Mo = g\mu_l^4(\rho_l - \rho_g)(\rho_l^2\sigma^3)^{-1}$ Morton number (ρ_l and ρ_g density of water and air, σ surface tension of water, g gravitational acceleration). Upper bar and $\langle\rangle$ denote averaging in time and space (radial direction), respectively. For $\langle\bar{d}_e\rangle$, value inside the parentheses denotes the SD

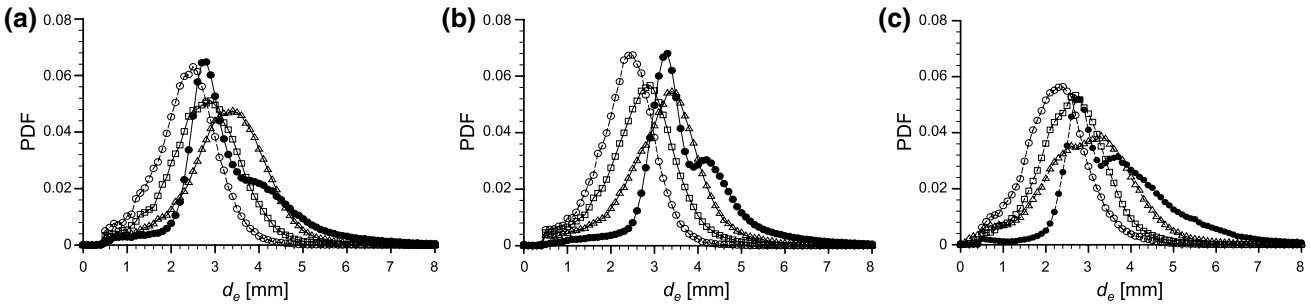

Fig. 4 Probability density function (PDF) of equivalent bubble diameter (d_e) at **a** $z/D = 4.5$; **b** 21; **c** 42: *opened circle* case 1; *opened square* case 2; *opened triangle* case 3; *filled circle* case 4

Table 1 summarizes the conditions of considered gas phase. From the case 1 to 4, the mean bubble diameter, $\langle\bar{d}_e\rangle$, gradually increases from 2.2 to 3.7 mm. The bubble Reynolds and Weber numbers based on $\langle\bar{d}_e\rangle$ and relative rise velocity are in the ranges of 600–880 and 2.0–2.9, indicating that the bubbles will be subjected to both the path (i.e., rising along oscillatory paths) and shape (i.e., deforming) instabilities. On the other hand, Fig. 4 shows the probability density function (PDF) of equivalent bubble diameter for each case. Here, the PDF is calculated by counting the number of bubbles whose d_e lies in each segmented range (width of 0.1 mm) and normalizing with the total number of bubbles. The equivalent bubble diameter is calculated for all the bubbles in individual instantaneous flow field (about 5×10^4 fields in total). It is seen that the bubble size at each vertical position is distributed in a narrow range, more or less centered at the mean value, and the differences between each case are established well. Also, the similar trend of PDFs at $z/D = 4.5$, 21, and 42 indicates that bubble coalescence does not occur frequently in the present experiment.

2.5 Uncertainties in the measurement

In measuring the flow statistics of gas and liquid phases with present method, there are some sources for experimental uncertainties. First, to evaluate the liquid velocity vector (u_{piv}), a magnification factor (M), time separation (Δt), and particle displacement (Δs) should be combined as $u_{piv} = M\Delta s/\Delta t$. Then, the percentage error [$\delta(u_{piv})$] in velocity measurement (Lawson et al. 1999) can be estimated by

$$\delta(u_{piv}) = \sqrt{\delta(M)^2 + \delta(\Delta s)^2 + \delta(\Delta t)^2}. \quad (1)$$

During calibration, the percentage error involved in magnification factor is estimated as 0.3 % with M of 0.6. The percentage error in time separation is less than 0.1 % with the operation of current high-speed camera. The pixel resolution that affects the particle displacement resolution is about 0.1 pixel which is about 2.2 % of the measured displacements. Therefore, the estimated uncertainty in the present velocity measurement is around 1.0 %. On the other hand, the perspective errors ($\varepsilon_{r,z}$: error in radial (r) or streamwise (z) direction) that show the influence of out-of-plane movement of tracking particles are expressed as:

$$\epsilon_{r,z} = \frac{\Delta l}{\Delta r, z}\tan\phi_{r,z}, \quad (2)$$

where Δl is the displacement (of seeding particles) of out-of-plane motion, $\Delta r,z$ is the measured displacement in radial (r) or streamwise (z) direction, and $\phi_{r,z}$ is the angle between the axis of lens and the line crossing the lens center and the particle (Adrian and Westerweel 2011). For

the present condition, the perspective errors in streamwise and radial directions are about 0.05 and 5 %, respectively, small enough not to affect the measurements significantly. Adrian and Westerweel (2011) have also commented that a single-camera PIV system would accompany acceptable experimental limit for the cases in which the principal flow direction lies within the plane of laser sheet, like the present condition. Here, the errors are estimated based on the observation that in the present measurements, Δl is comparable to Δr that is about 5 % of Δz. In addition, the circular curvature of the pipe (although a rectangular jacket wraps it) makes the particle image to be shifted. Generally, the magnitude of the shift is zero at the pipe center but is about 0.1 mm at $r/D = 0.45$ (Zhou et al. 2013).

In detecting individual bubble, the displacement of bubble motion is measured approximately one-fourth of the bubble diameter, and the number of bubbles in one image is about 3–7 for the cases 1–3. Here, the uncertainties in the measured bubble velocity estimated at 95 % confidence level are about 2.5 %, while the measured void fraction, bubble diameter, and aspect ratio have the uncertainties of 3.7, 6.5, and 3.7 %, respectively.

3 Results and discussion

3.1 Instantaneous flow fields

Before we discuss the detailed flow statistics, let us investigate the variation of instantaneous flow fields, which is one of the advantages of using an optical image-based measurement. As introduced earlier, there are a few studies that utilized a similar two-phase particle image velocimetry method to investigate the bubble-induced turbulence with instantaneous flow fields (Fujiwara et al. 2004; Liu et al. 2005; Pang and Wei 2013). This is because mostly due to the difficulties in accurately separating the gas and liquid phases from the acquired images and also distinguishing and tracking the overlapped bubbles. To overcome this, based on the methods suggested by Lindken and Merzkirch (2002) and Bröder and Sommerfeld (2007), we spent much effort in optimizing the hardware setup (Sect. 2.2) and image processing algorithm (Sect. 2.3). Among previous studies, Fujiwara et al. (2004) measured the distributions of void fraction and bubble rise velocity, while analyzing instantaneous fluctuating vorticity fields and turbulent energy budget. Liu et al. (2005) measured the bubble trajectory and visualized the corresponding liquid-phase flow structures in single-bubble chain flows. They characterized the variations of turbulence intensity and turbulent stress profiles depending on the bubble trajectory, i.e., straight and oscillatory. Pang and Wei (2013) provided the contour of turbulence intensities and further analyzed the bubble-induced flow structures using POD technique in a two-dimensional channel flow laden with small dispersed bubbles. Compared to these studies, we try to simultaneously measure various aspects of gas and liquid flow and analyze them as a whole. Furthermore, the information obtained from analyzing the instantaneous flow fields is adopted to derive a new two-phase turbulent stress model (see Sect. 3.4).

Figures 5 and 6 show the representative instantaneous flow fields with velocity vectors (gas and liquid phases) and a spanwise vorticity (ω) contour (liquid phase). Here, the spanwise vorticity is calculated by subtracting the time-averaged vorticity of single-phase laminar flow from the instantaneous vorticity of two-phase flow. At each instant, the shape and velocity of each bubble are captured well in addition to the flow structures induced by those bubbles. Considering that most of previous studies have reported the flow statistics without the information about instantaneous flow fields, this is worth investigating in detail. At $z/D = 4.5$, for the case 2 in which the mean void fraction is relatively low, the flow structures induced by individual bubble motion are retained for a relatively long duration (denoted as an open arrow) (Fig. 5a), while the interaction between bubble wakes appears for higher $\langle\bar{\alpha}\rangle$ (denoted as an open arrow in Fig. 5b). On the other hand, for the case 3 only, interestingly it is observed that the liquid flows downward locally where there are less bubbles (highlighted as a dashed box in Fig. 5b). As the flow develops (at $z/D = 21$), it is observed that the bubble distribution becomes more or less symmetric (Fig. 5c, d). For the case 2, however, still the vortical structure induced along individual bubble path retains its characteristics (Fig. 5c).

As shown in Fig. 6, at $z/D = 42$, general pictures of the bubble dynamics are similar to those at $z/D = 21$ in Fig. 5c, d. For all cases, the dominant behavior of rising bubbles is a two-dimensional zigzag motion (or sometimes three-dimensional helical one), which is expected from the conditions of present bubbles (Table 1). Once the bubble is captured, its trajectory does not disappear in the field of view, indicating that the effect of out-of-plane motion would be small. Also, it is clear that the bubble-induced flow structures become more complex as $\langle\bar{\alpha}\rangle$ increases. For the cases 1 and 2, due to the relatively small void fraction, the substantial bubble-induced liquid velocity is confined near the bubble and the vortical structures due to individual bubble wake are retained for some time (denoted as open arrows in Fig. 6a, b). As the void fraction increases, the events of bubble–bubble interaction occur more frequently, which results in the modification of bubble wake and more complicated bubble-induced flow structures. When the mean volume void fraction is small (cases 1 and 2), it does not happen frequently that the bubbles' trajectories cross each other, i.e., trajectory of one bubble is not affected by the wake of other bubbles

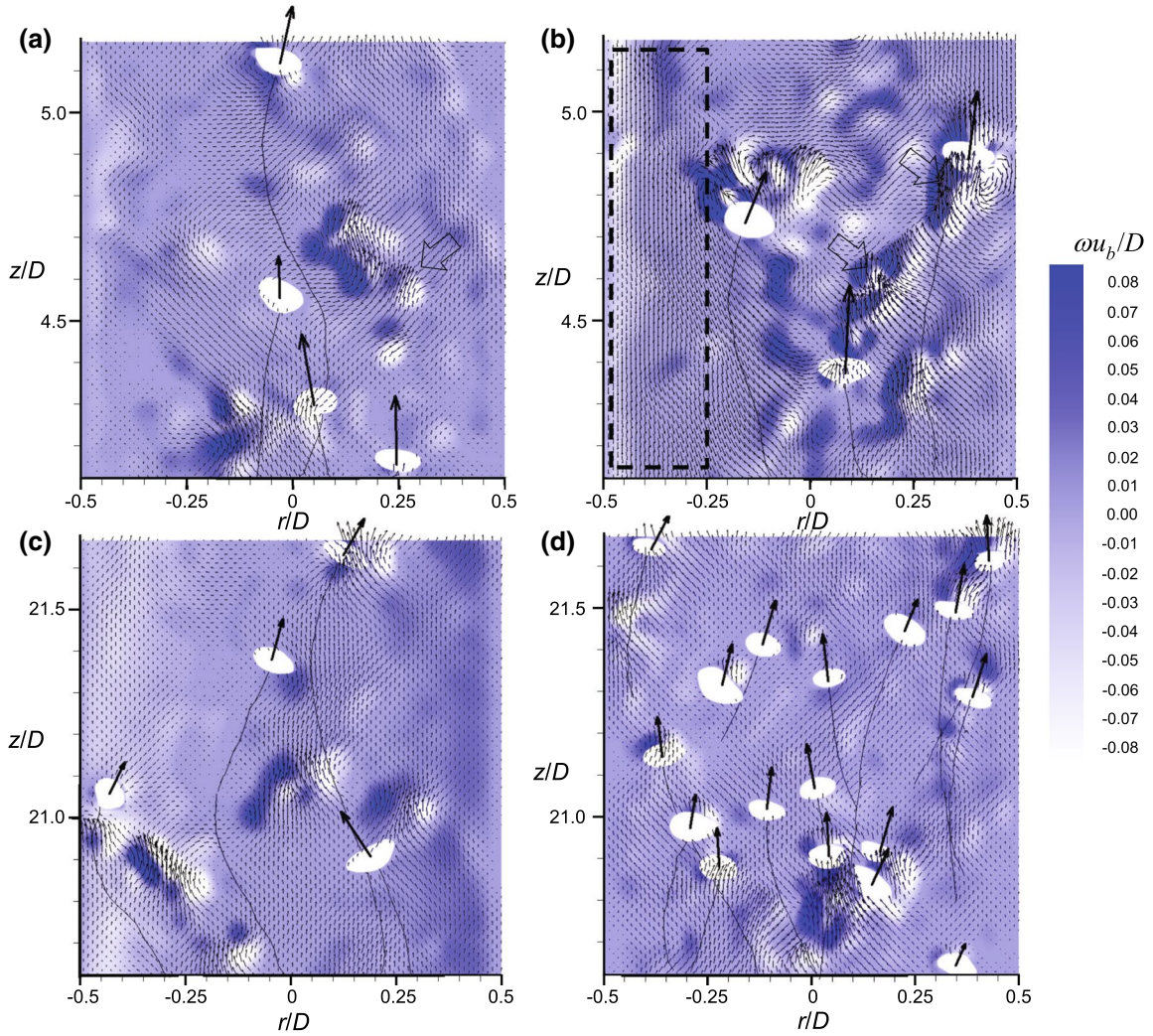

Fig. 5 Instantaneous flow fields with velocity vectors (gas and liquid phases) and a contour of spanwise vorticity (ω) for laminar bubbly flow: **a** case 2 and *b* case 3 measured at $z/D = 4.5$; **c** case 2 and **d** case 4 measured at $z/D = 21$. *Solid lines* denote the rising path of individual bubble

(Fig. 6a, b). However, as shown in Fig. 6c, d, bubbles tend to affect the trajectories each other. Furthermore, the vortical structures induced by bubbles are confined to a proximity of them for the cases 1 and 2 (Fig. 6a, b); however, stronger signatures from the wake–wake interactions remain in the flow, for higher mean void fractions (highlighted as a dashed box, for example, in Fig. 6d).

3.2 Bubble characteristics

The radial distributions of local void fraction for the cases 1–4 are plotted in Fig. 7. Here, the local void fraction is defined as the portion of the area occupied by the bubbles in the area of rectangular segment whose width (Δr) is $0.025D$ and height is $1D$, which are calculated by averaging more than 5×10^4 instantaneous flow fields, at the center plane (see Fig. S3 in the supplementary material). As introduced, we intentionally introduce asymmetrically distributed bubbles at the inlet, which is evidenced by the void distribution near the inlet (Fig. 7a). The void distribution becomes more or less symmetric as the flow develops due to bubble-induced mixing and wall-peaking profiles are achieved for the cases 1–3 while intermediate peaking (a transient state between wall and core peakings) is observed for the case 4 with the highest $\langle\bar{\alpha}\rangle$ (Fig. 7b, c). Since the dispersion of bubble due to mixing would be negligible in laminar flow, the achievement of a symmetric bubble distribution before the entrance length ($37.5D$) of single-phase flow indicates that the mixing by bubble-induced agitation (or shear-induced migration) has a stronger influence than the single-phase flow development. For wall-peaking distributions, the location of maximum void peak moves from $|r/D| \simeq 0.4$ to 0.35 with increasing $\langle\bar{\alpha}\rangle$ and $\langle\bar{d}_e\rangle$.

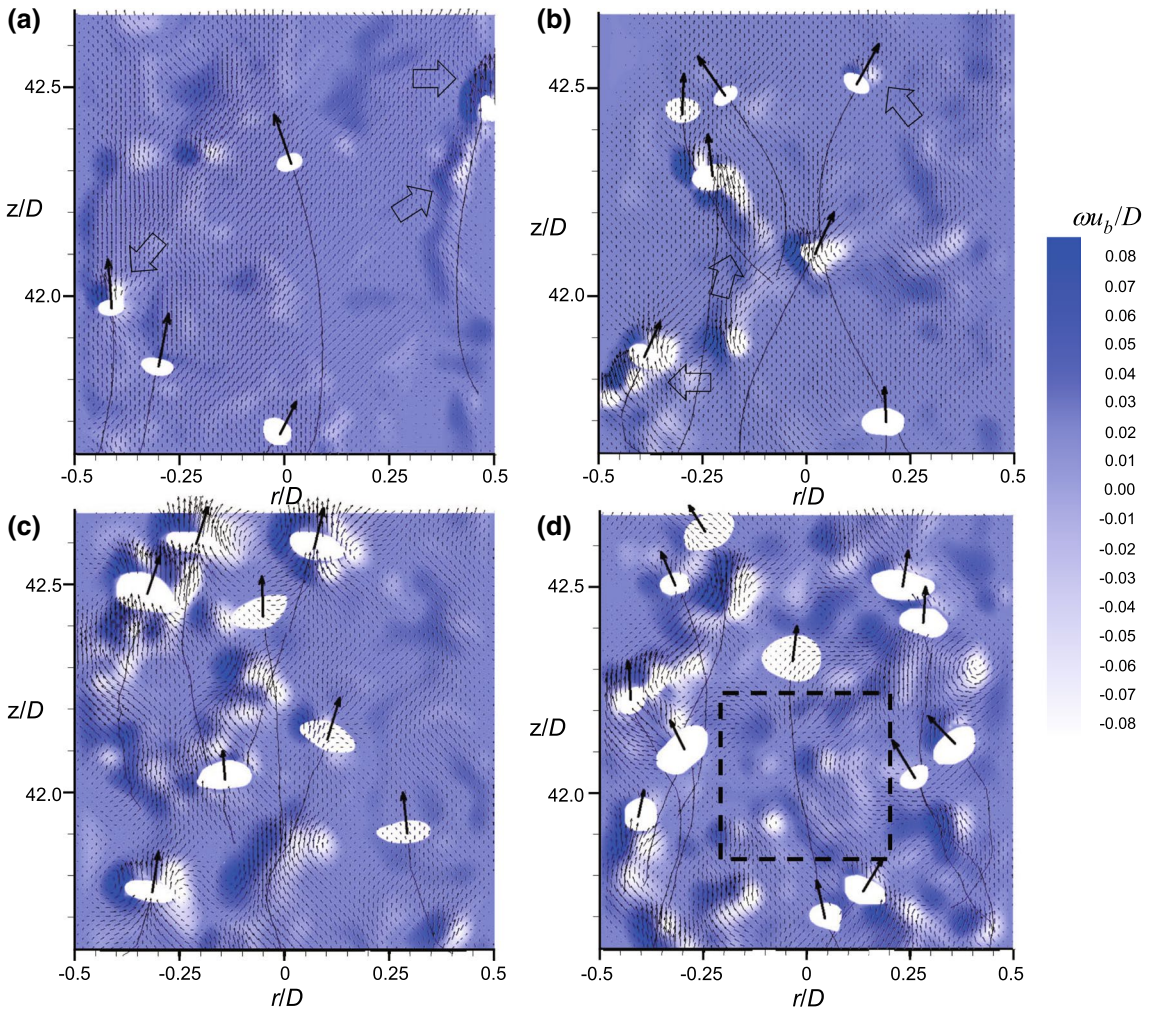

Fig. 6 Instantaneous flow fields with velocity vectors (gas and liquid phases) and a contour of spanwise vorticity (ω) for laminar bubbly flow measured at $z/D = 42$: *a* case 1; *b* case 2; *c* case 3; *d* case 4. *Solid lines* denote the rising path of individual bubble

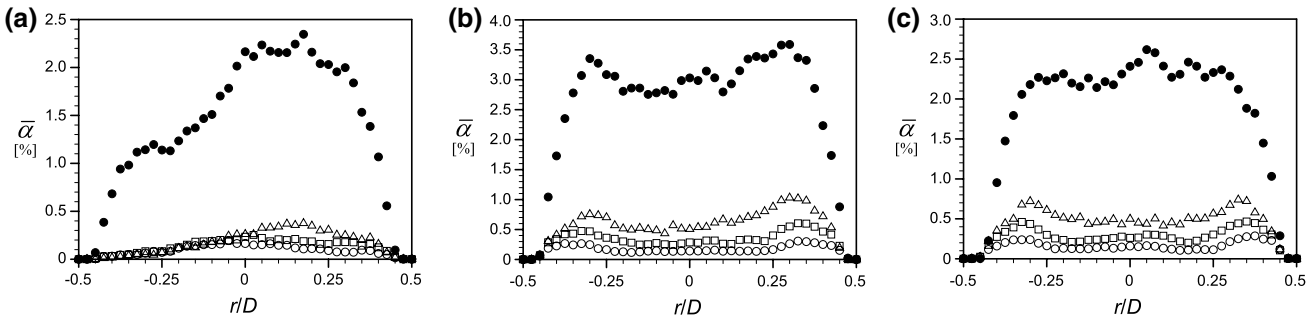

Fig. 7 Radial distributions of local void fraction ($\bar{\alpha}$) at **a** $z/D = 4.5$; **b** 21; **c** 42: *opened circle* case 1, *opened square* case 2, *opened triangle* case 3, *filled circle* case 4

In fact, the void distribution is related to the distributions of bubble size and frequency, as shown in Fig. 8a, b, respectively. At all z/D's, for the cases 1–3, the bubble size has a relatively flat distribution at core region (defined up to the position of the maximum $\bar{\alpha}$ of wall-peaking profiles), while the case 4 has a slight gradient and a narrower plateau at the core region (Fig. 8a). Approaching the wall, the bubble size decreases sharply,

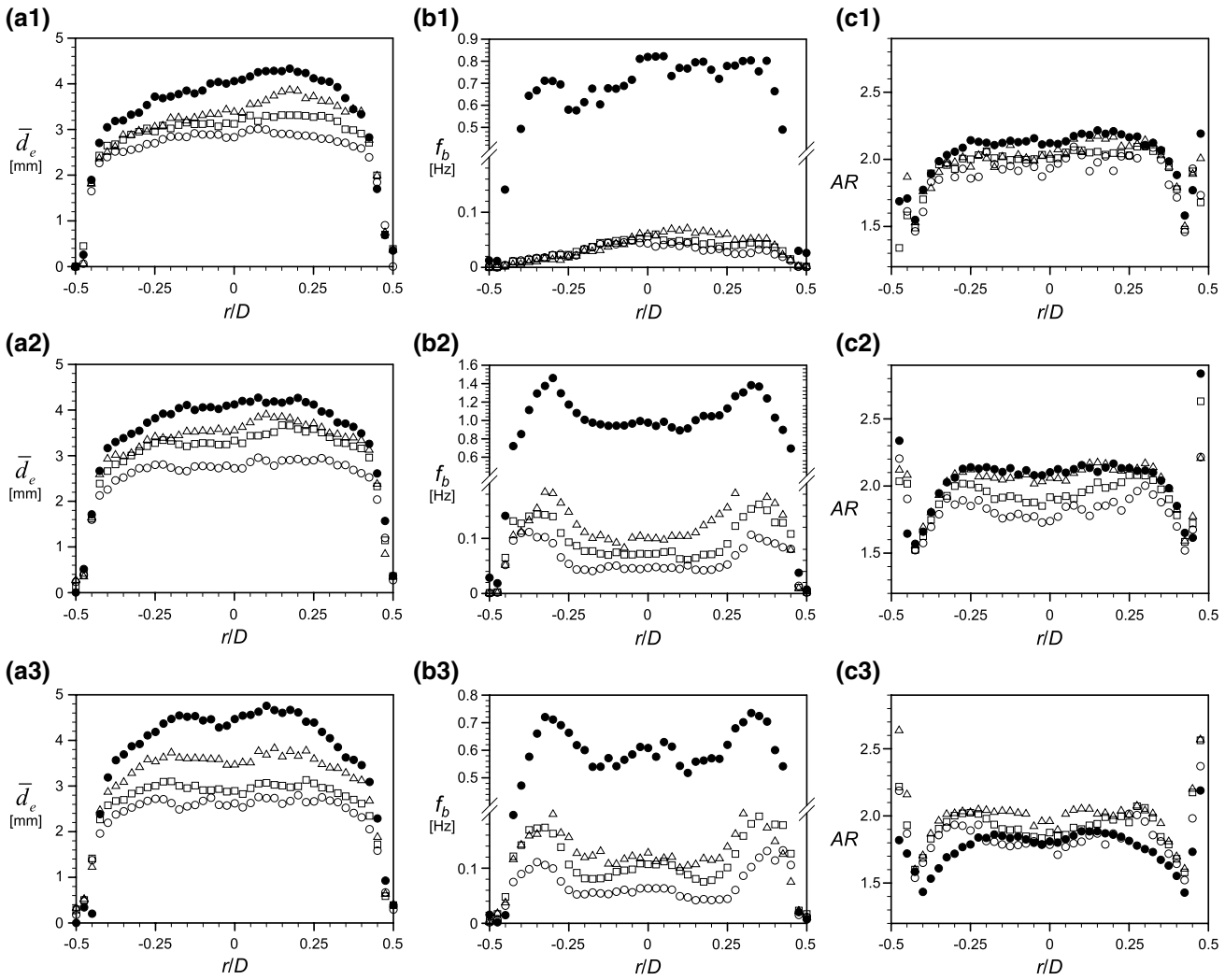

Fig. 8 Radial distributions of equivalent bubble diameter ($\bar{d}_e$), bubble frequency (f_b), and aspect ratio (AR) at $z/D = 4.5$ (**a1**, **b1**, **c1**); 21 (**a2**, **b2**, **c2**); 42 (**a3**, **b3**, **c3**): *opened circle* case 1, *opened square* case 2, *opened triangle* case 3, *filled circle* case 4

indicating that small bubbles ($\lesssim$2 mm) mostly migrate to the wall. This is somehow different to the observation by Michiyoshi and Serizawa (1986) in which the bubble size distribution shows a small peak near the wall, like the void profile. The bubble frequency, defined as the averaged number of bubbles that pass the specific location in a given time span (Shawkat et al. 2008), in general, follows the same trend (i.e., peaking condition) as the void profiles (Fig. 8b). For example, at $z/D = 42$, the bubble frequency of case 4 has a peak at the core in addition to the wall peaks (Fig. 8b3) like the void distribution in Fig. 7c.

While the present void distribution can be understood further through analyzing the lateral forces acting on a rising bubble [see the supplementary material and the recent review by Tryggvason and Lu (2015)], Adoua et al. (2009) proposed that the sign of shear-induced lift (lateral) force on an oblate bubble is determined by the bubble aspect ratio (AR) for bubble Reynolds number of $\boldsymbol{O}(10^2$–$10^3)$ under a small shear rate. In their simulation, a bubble tends to migrate toward the higher liquid velocity region when $AR \lesssim 2.2$ while it is reversed at $AR \gtrsim 2.2$. Since the present bubble Reynolds number (Table 1) and shear rate $\sim$0.03–0.04) is similar to those of Adoua et al. (2009), it is possible to explain the void distribution based on their argument. As shown in Fig. 8c, the present bubble AR shows a plateau (at a value smaller than about 2.1) in the core region, has a minimum peak at $|r/D| \simeq 0.35 - 0.4$, and then increases sharply (larger than 2.2) at $|r/D| > 0.4$. Since the wall-normal force (acting toward the core region) decreases with decreasing AR (at $AR \leq 2.2$) (Adoua et al. 2009), the bubble AR near the wall-peaking position becomes the minimum where the lateral forces acting on bubbles are balanced.

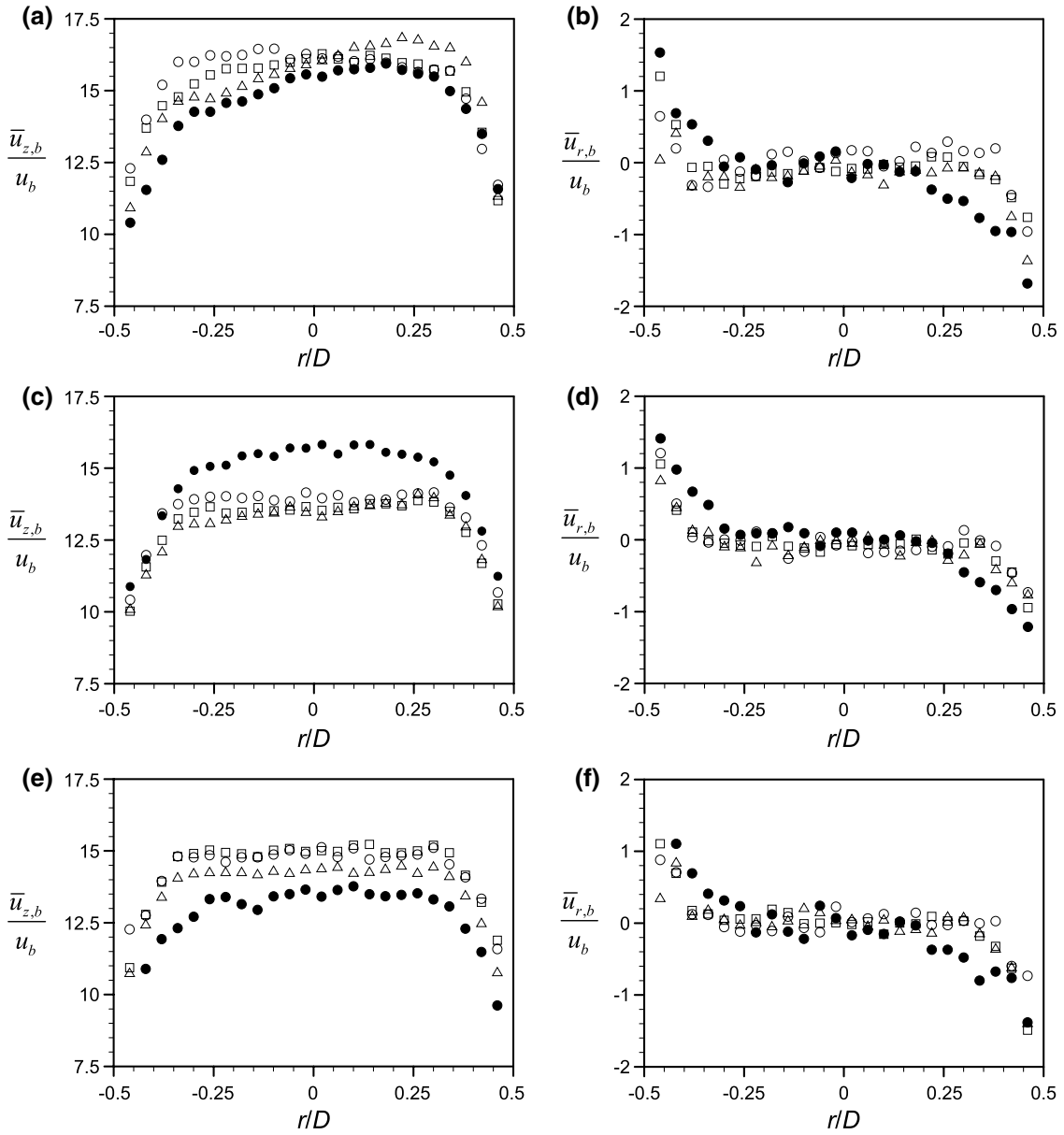

Fig. 9 Radial variations of mean bubble velocity normalized by the bulk velocity (u_b) of single-phase flow: **a**, **c**, **e** vertical velocity ($\bar{u}_{z,b}$); **b**, **d**, **f** radial velocity ($\bar{u}_{r,b}$). Measured locations are $z/D = 4.5$ (**a**, **b**), 21 (**c**, **d**), and 42 (**e**, **f**). *Opened circle* case 1, *opened square* case 2, *opened triangle* case 3, *filled circle* case 4

Figure 9 shows the distributions of mean bubble velocity in vertical ($\bar{u}_{z,b}$) and radial ($\bar{u}_{r,b}$) directions, normalized by the bulk velocity (u_b) of single-phase flow. In the core region ($|r/D| \lesssim 0.35$–0.4), both $\bar{u}_{z,b}$ and $\bar{u}_{r,b}$ have a flat distribution, while the vertical velocity tends to decrease with increasing $\langle\bar{\alpha}\rangle$, but the radial velocity is scattered around zero without specific dependency on $\langle\bar{\alpha}\rangle$. Near the wall, the rise velocity decreases sharply but the wall-normal velocity increases greatly, which agrees with the wall-peaking void profiles (Fig. 7). Compared to the rise velocity, the radial velocity is very small (below 5 %) and is not affected much by $\langle\bar{\alpha}\rangle$. As shown in Figs. 5, 6, the interactions between bubbles are not frequent (cases 1–2, in particular) and thus the rising behavior (mostly two-dimensional zigzag motion) of individual bubble is retained in most cases. Thus, $\bar{u}_{r,b}$ is almost zero at the core region and the increase at the wall region is caused by the shear (wall)-induced migration.

The bubble rise velocity is higher than the liquid velocity (due to buoyancy); however, it is interesting that $\bar{u}_{z,b}$ is larger than 10 times the single-phase bulk velocity (Fig. 9a, c, e). Based on the phasewise momentum conservation

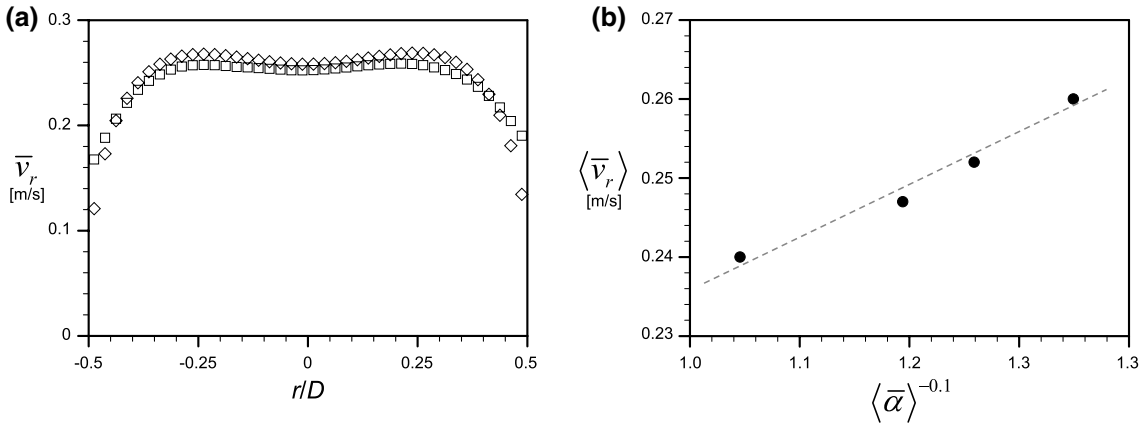

Fig. 10 **a** Comparison of estimated (*opened diamond*) averaged relative bubble rise velocity ($\langle \bar{v}_r \rangle$) with the present measurement (*opened square*) for the case 2 measured at $z/D = 42$. **b** Scaling relation between $\langle \bar{v}_r \rangle$ and $\langle \bar{\alpha} \rangle$

equations and the assumption of zero gradient of pressure and stress at the bubble interface, Ishii and Zuber (1979) have suggested the relative bubble rise velocity ($v_r = u_{z,b} - u_z$) as:

$$v_r|v_r| = \frac{8}{3}\frac{0.5d_e}{C_D\rho_l}(\rho_l - \rho_g)g(1-\alpha), \tag{3}$$

where C_D is drag coefficient. Since the present bubbles slightly deform during rising, C_D is estimated using the formulation (Eq. 4) derived for a distorted particle regime based on the mixture viscosity model (Ishii and Zuber 1979).

$$\left.\begin{aligned} C_D &= \tfrac{2}{3}d_e\sqrt{\tfrac{g(\rho_l-\rho_g)}{\sigma}}\left(\tfrac{1+17.67f(\alpha)^{6/7}}{18.67f(\alpha)}\right)^2 \\ f(\alpha) &= \sqrt{1-\alpha}(\alpha)^{2.5(\mu_g+0.4\mu_l)/(\mu_g+\mu_l)} \end{aligned}\right\} \tag{4}$$

Here, μ_g and μ_l are the viscosity of air and water, respectively. For the present condition in which μ_g is much smaller than μ_l, as commented by Ishii and Zuber (1979), it is noted that μ_g should have a negligible influence on the mixture viscosity and eventually on the modeled C_D in Eq. 4. Since the wall proximity affects the migration of bubbles significantly (Jeong and Park 2015), we additionally consider it using the relation by Uno and Kintner (1956) as below:

$$\frac{v_{r,wall}}{v_r} = \left[\frac{1}{0.83}\left(1-\frac{d_e}{D}\right)\right]^{0.765}. \tag{5}$$

Applying Eqs. 3–5 to the present condition at $z/D = 42$, the relative bubble rise velocity is estimated as $\langle \bar{v}_r \rangle = 0.254$, 0.252, 0.249, and 0.245 ms^{-1} for the cases 1–4, respectively, while the measured values are 0.260, 0.252, 0.247, and 0.240 ms^{-1}, which shows a good agreement (within 2 %). In addition, the radial distribution of rise velocity is also predicted well with the considered models, as shown in Fig. 10a. It is noted that the prediction fails to provide a reasonable result if one of the conditions such as deformability and wall effect is not considered properly.

As noticed, $\langle \bar{v}_r \rangle$ is found to decrease with increasing $\langle \bar{\alpha} \rangle$. Previously, Riboux et al. (2010) have suggested that $\langle \bar{v}_r \rangle$ scales with $\langle \bar{\alpha} \rangle^{-0.1}$, based on the measurements of homogeneous bubble columns [bubble Reynolds number of $\boldsymbol{O}(10^2$–$10^3)$]. In Fig. 10b, the mean bubble rise velocity relative to the liquid velocity for the cases 1–4 is plotted against $\langle \bar{\alpha} \rangle^{-0.1}$. As shown, the present bubbles rising in a laminar flow follow the same scaling relation of $\langle \bar{v}_r \rangle \sim \langle \bar{\alpha} \rangle^{-0.1}$. We will use this relation to develop a new model for two-phase turbulent stress (see Sect. 3.4).

3.3 Liquid velocity and turbulence statistics

Figure 11 shows the mean liquid velocity in vertical ($\bar{u}_z$) and radial ($\bar{u}_r$) directions, together with the theoretical parabolic profile for Hagen–Poiseuille flow and that measured for a single-phase turbulent flow at $Re_D = 10^4$ ($Re_\tau \simeq 350$). At $z/D = 4.5$, $\bar{u}_z$ is mostly determined by the distribution of $\bar{\alpha}$ (Fig. 11a); liquid flow is accelerated where more bubbles are populated but is decelerated with less bubbles. Although this trend is not noticeable for the case 1 that has the smallest $\langle \bar{\alpha} \rangle$ among considered, the dependence on the void distribution becomes clear with increasing $\langle \bar{\alpha} \rangle$ (highlighted with arrows). As shown in Fig. 5b, liquid flows downward (i.e., backward) locally due to the asymmetric bubble accumulation for the case 3, which disappears as $\langle \bar{\alpha} \rangle$ increases further. At $z/D = 21$, the vertical velocity has a similar trend as that at $z/D = 4.5$ (Fig. 11c), although the void distribution changes to a wall-peaking profile (Fig. 7b). From a direct numerical simulation of laminar bubbly upward flow in a vertical channel, Tryggvason and Lu (2015) also found that the bubbles at the transient (i.e., developing) stage move to the

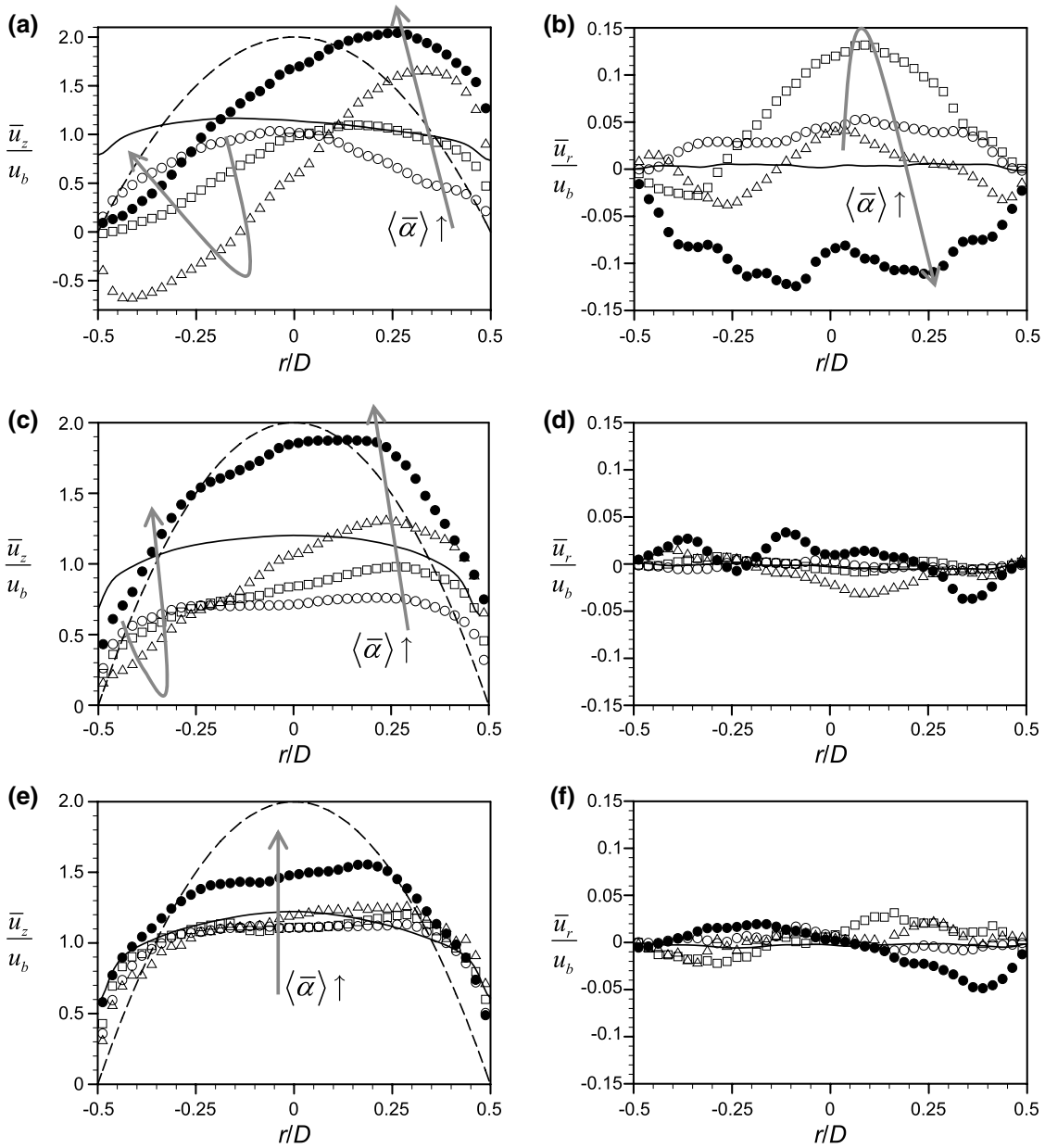

Fig. 11 Radial variations of mean liquid velocity normalized by the bulk velocity (u_b) of single-phase flow: **a**, **c**, **e**) vertical velocity ($\bar{u}_z$); **b**, **d**, **f**) radial velocity ($\bar{u}_r$). Measured locations are $z/D = 4.5$ (**a**, **b**), 21 (**c**, **d**), and 42 (**e**, **f**). *Opened circle* case 1; *opened square* case 2, *opened triangle* case 3, *filled circle* case 4; *dashed lines*, theoretical profile for Hagen–Poiseuille flow; *solid lines*, data for single-phase flow measured at $Re_D = 10^4$. *Arrows* in the plot denote the direction of increasing $\langle\bar{\alpha}\rangle$

walls quickly with the liquid velocity being unaffected. The liquid velocity retains the asymmetric profile (the difference among the cases 1–3 is reduced) even with a symmetric void distribution, because the bubble rise velocity is much faster than the liquid velocity. When the flow fully develops (Fig. 11e), $\bar{u}_z$ has a flat distribution at the core region, while it is sharply reduced toward the wall, which has been reported previously (Antal et al. 1991; Kashinsky et al. 1993; Lu et al. 2006; Hosokawa and Tomiyama 2013). Compared to the theoretical profile for single-phase laminar flow, the liquid flow is slowed down at the core region but moves faster near the wall. For relatively small $\langle\bar{\alpha}\rangle$'s (cases 1–2), the liquid velocity profiles roughly collapse to one curve which matches well, especially the velocity gradient near the wall, with that of the single-phase turbulent flow at $Re_D = 10^4$. It is interesting to see that the liquid velocity induced by small number of bubbles resembles the turbulent flow. As $\langle\bar{\alpha}\rangle$ increases further (case 4), however, the liquid velocity profile deviates from the turbulent profile.

Compared to $\bar{u}_z$, the magnitude of $\bar{u}_r$ is negligibly small, possibly due to the fact that the dominant movement of present bubbles is a zigzag motion and the events of bubble–bubble interaction (e.g., collision) are not observed frequently. In particular, this is more clear at fully developed regime (at $z/D = 42$) where the bubble distribution is quasi-steady, and the specific dependency of $\bar{u}_r$ on $\bar{\alpha}$ is not observed (Fig. 11f). At developing regime, however, $\bar{\alpha}$ and $\bar{u}_r$ are dependent on each other. At $z/D = 4.5$, radial velocity is mostly positive for the cases 1–3, which increases with increasing $\langle\bar{\alpha}\rangle$ (Fig. 11b). This would induce bubbles to migrate toward the right-hand side wall ($r/D = 0.5$), as shown in Fig. 7a. As $\langle\bar{\alpha}\rangle$ increases further (case 4), on the other hand, a negative $\bar{u}_r$ in case 4 induces the bubbles to move to the left-hand side and results in an increment of the void fraction there. Thus, as shown in Fig. 7a, $\bar{\alpha}$ at the left-hand side ($-0.5 < r/D < -0.25$) has also increased substantially. At $z/D = 21$ where the void distribution for the cases 1–4 has become more or less symmetric, $\bar{u}_r$ decreases

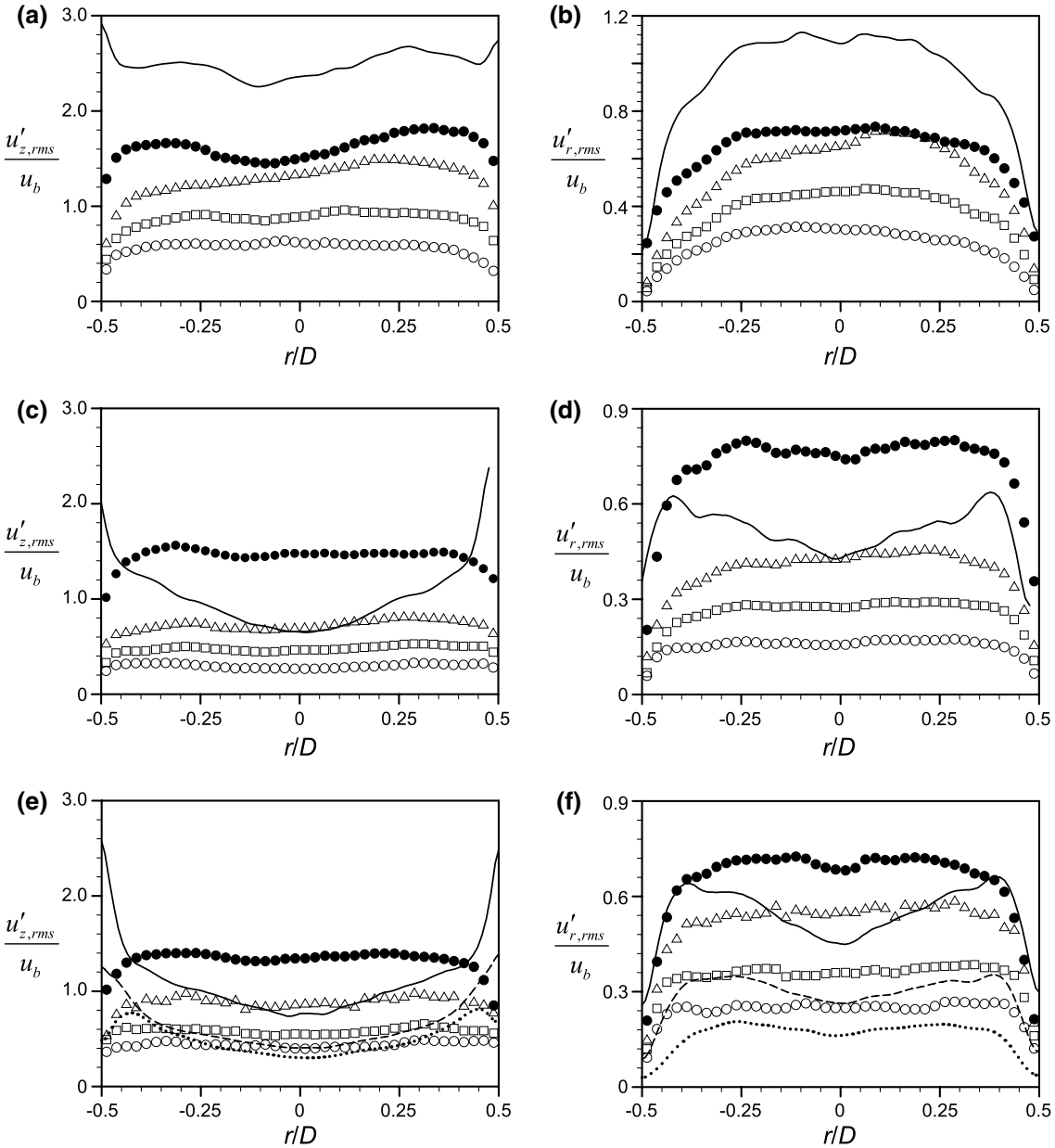

Fig. 12 Radial variations of root-mean-square of velocity fluctuation in liquid phase normalized by the bulk velocity (u_b) of single-phase flow: **a**, **c**, **e** vertical velocity ($u'_{z,rms}$); **b**, **d**, **f** radial velocity ($u'_{r,rms}$). Measured locations are $z/D = 4.5$ (**a**, **b**), 21 (**c**, **d**), and 42 (**e**, **f**). *Opened circle* case 1, *opened square* case 2, *opened triangle* case 3, *filled circle* case 4, data for single-phase flow measured at $Re_D = 3 \times 10^3$ (*dotted lines*), 5×10^3 (*dashed lines*), and 10^4 (*solid lines*)

significantly and has no specific relation with $\bar{\alpha}$ (Fig. 11d), similar to that at $z/D = 42$.

Figures 12 and 14 show the liquid-phase turbulence. Velocity fluctuations in a single-phase turbulent flow at $Re_D = 10^4$ are also plotted together at all locations, and it is noted that they are also normalized with the bulk velocity of the single-phase laminar flow, to avoid the situation in which the trend of varying turbulence is buried by normalizing with its large (about 10 times) bulk velocity. Figure 12 shows the bubble-induced liquid velocity fluctuations (i.e., normal stress) in vertical ($u'_{z,rms}$) and radial ($u'^{r,rms}$) directions. At the fully developed regime ($z/D = 42$), data for single-phase flows at $Re_D = 3 \times 10^3$ and 5×10^3 are added to be compared with the trend of bubble-induced turbulence in more detail. Even with small void fractions, it is clear that the bubbles induce a substantial turbulence both in the core and in the wall regions, which gets stronger with increasing $\langle\bar{\alpha}\rangle$. Note that $u'_{z,rms}$ and $u'_{r,rms}$ are nominally zero for the laminar (i.e., background) flow. At $z/D = 4.5$, $u'_{z,rms}$ for the cases 1–2 shows a flat distribution with a slight decreases near the wall, while for larger $\langle\bar{\alpha}\rangle$ (cases 3–4), it shows a distribution similar to that of $\bar{\alpha}$, i.e., higher $u'_{z,rms}$, where there are more bubbles (Fig. 12a). $u'_{r,rms}$ shows a similar trend on $\langle\bar{\alpha}\rangle$, but decreases at the wall region more sharply showing a more or less parabolic profile (Fig. 12b). As the flow develops, for all $\langle\bar{\alpha}\rangle$'s considered, both $u'_{z,rms}$ and $u'_{r,rms}$ tend to have a plateau at the core and a decrease toward the wall, which is observed most clearly at $z/D = 42$ (Fig. 12c–f). Unlike the single-phase turbulent pipe flow (Westerweel et al. 1996), it is interesting to see that bubble-induced $u'_{z,rms}$ and $u'_{r,rms}$ show the similar profile, which has been also reported previously (Wang et al. 1987; Liu and Bankoff 1993; Fujiwara et al. 2004; Hosokawa and Tomiyama 2013). As shown, the bubble-induced turbulence does not follow the same trend of present local void distribution, e.g., a wall-peaking profile at $z/D = 24$ and 42 (Fig. 7b, c). These phenomena have been also reported for laminar (Lu et al. 2006; Hosokawa and Tomiyama 2013) and turbulent (Sato and Sekoguchi 1975; Michiyoshi and Serizawa 1986; Liu and Bankoff 1993) bubbly flows. On the contrary, other studies have shown that two-phase flow turbulence intensity shows a wall-peaking profile, when the Reynolds number of background flow is relatively high (Serizawa et al. 1975; Wang et al. 1987; Liu and Bankoff 1993; Fujiwara et al. 2004; Shawkat et al. 2008). This indicates that in two-phase turbulence, the shear-induced turbulence becomes more influential at the wall region with increasing liquid velocity.

Hosokawa and Tomiyama (2013) reported that the ratio between $u'_{z,rms}$ and $u'_{r,rms}$ is 2:1 from their LDV measurement. The same relation also holds for the present data for all z/D's considered. It is further thought that due to the oscillating bubble paths, the bubble-induced turbulence in radial direction is comparable to that in vertical direction, although the mean liquid velocity is dominantly oriented to the vertical direction.

In general, the shape of bubble-induced turbulence profile resembles that of single-phase turbulent flow at $z/D = 4.5$ (Fig. 12a, b), but they show different trend as the flow develops. As shown in Fig. 12c–f, the single-phase turbulence has a convex profile at the core region and a peak at the wall region, but the bubble-induced $u'_{z,rms}$ and $u'_{r,rms}$ have a wide plateau at the core and do not have a wall peak. Quantitatively, at $z/D = 4.5$, the bubble-induced turbulence levels for the cases 1–4 are smaller than those of a single-phase turbulent flow (e.g., $Re_D = 10^4$; Fig. 12a, b), but as the flow develops, bubble-induced turbulence becomes stronger or comparable, depending on $\langle\bar{\alpha}\rangle$ (Fig. 12c–f). In the core region, bubble-induced turbulence becomes larger than (or comparable to) the single-phase turbulence at higher Re_D with increasing $\langle\bar{\alpha}\rangle$. On the other hand, bubble-induced $u'_{z,rms}$ is smaller than the single-phase turbulent flow at the wall region (Fig. 12e). This is because bubbles near the wall (wall peak) strongly reduce the velocity fluctuations there, while in the core region where the shear-induced turbulence generation for the single-phase turbulent flow is low, substantial velocity fluctuations are generated by the bubble wakes (So et al. 2002; Fujiwara et al. 2004). Unlike $u'_{z,rms}$, interestingly, the near-wall gradient of $u'_{r,rms}$ matches well with the single-phase turbulent flow (Fig. 12f). Considering that the contribution of shear-induced turbulence is almost negligible in the present condition, the turbulence intensity profile in Fig. 12 represents the characteristics of bubble-induced turbulence.

On the other hand, the range of Reynolds numbers ($0.3–1 \times 10^4$) for single-phase turbulent flow to compare with the bubble-induced turbulence is actually determined (limited) by the capacity of our experimental setup. However, based on the trend of increasing single-phase flow turbulence with increasing Re_D, it is expected that the turbulence at the Reynolds numbers higher than 10^4 would be larger than the bubble-induced turbulence with considered range of $\langle\bar{\alpha}\rangle$. Thus, it would be very interesting, as a future research, to investigate whether the bubble-induced turbulence at higher $\langle\bar{\alpha}\rangle$ matches with the single-phase turbulence at higher Re_D.

As shown, the bubble-induced turbulence increases with increasing $\langle\bar{\alpha}\rangle$ (Fig. 12), and a scaling relation between the bubble-induced turbulence (normal stress) and $\langle\bar{\alpha}\rangle$ has been proposed (Risso and Ellingsen 2002; Riboux et al. 2010). They showed that the vertical components in liquid velocity fluctuation scale with $\langle\bar{\alpha}\rangle^{0.4}$ in a homogeneous bubble swarm. In Fig. 13, we have examined whether such scaling relation is valid for the present cases. When the flow is developing, the vertical liquid velocity fluctuation does not show a specific trend, but it scales well with the mean void

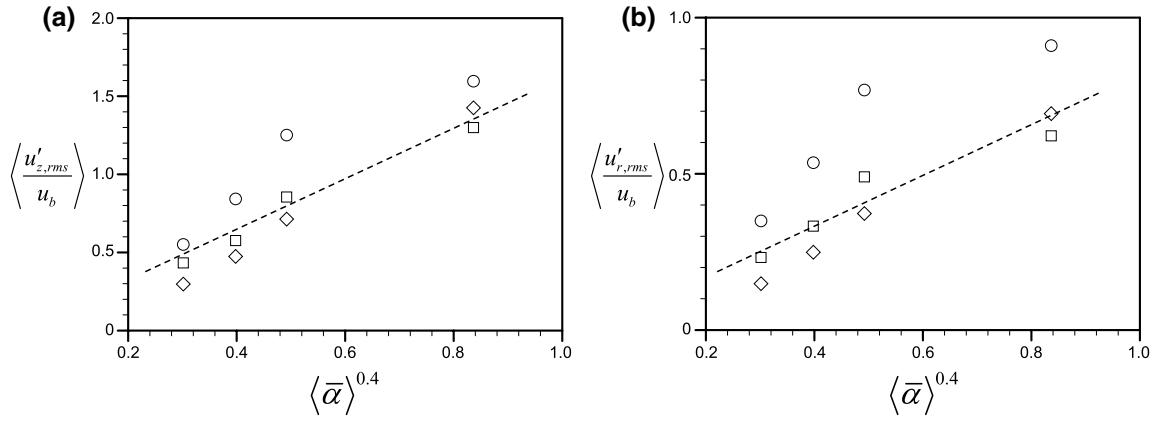

Fig. 13 Scaling relation between bubble-induced liquid velocity fluctuation and $\langle \bar{\alpha} \rangle$: **a** vertical velocity fluctuation; **b** radial velocity fluctuation. *Opened circle* at $z/D = 4.5$, *opened diamond* 21, *opened square* 42. *Dashed lines* in each figure are drawn to cross the origin (i.e., zero velocity fluctuation at $\langle \bar{\alpha} \rangle = 0$)

fraction as $\langle u'_{z,rms} \rangle \sim \langle \bar{\alpha} \rangle^{0.4}$, as the bubbly flow enters into a fully developed regime (Fig. 13a). Since Riboux et al. (2010) have provided the data for more or less at a quasi-steady state, we think the present data somehow show how the evolution in the two-phase flow interaction shows up in the turbulence intensity. Interestingly, it is found that the radial velocity fluctuation also scales with $\langle \bar{\alpha} \rangle^{0.4}$ (Fig. 13b) and the scaling relation becomes clearer as the flow develops. We think this information will be useful in modeling the bubble-induced turbulence (normal stress).

Radial distribution of Reynolds stress ($-\overline{u'_z u'_r}$) normalized by the bulk velocity of the single-phase flow is plotted in Fig. 14. At $z/D = 4.5$, except the case 1, bubbles induce an enhancement of Reynolds stress at the core region, while it is affected little near the wall (Fig. 14a). At this position, the void distribution has a hat-like profile whose peak is slightly skewed to the right-hand side (Fig. 7a), and the enhanced Reynolds stress is more pronounced where more bubbles are accumulated. As the flow develops, the Reynolds stress profile changes into two types: For small $\langle \bar{\alpha} \rangle$ (cases 1 and 2), the Reynolds stress profile shows a 'double-S' shape that has secondary peaks in the core region (dashed arrow in Fig. 14c) in addition to the main peaks at the wall region (solid arrow). For higher $\langle \bar{\alpha} \rangle$ (cases 3 and 4), it resembles the well-known profile ('single-S' shape) of single-phase turbulent flow, where the main peaks exist only (Fig. 14c). As $\langle \bar{\alpha} \rangle$ increases, the peak of Reynolds stress increases as well. Interestingly, the Reynolds stress of the case 4 is close to that of a single-phase turbulent flow at $Re_D = 10^4$ (Fig. 14c). This indicates that in nature the bubble-induced turbulence is very similar to the turbulence of single-phase turbulent flow (i.e., shear-induced turbulence). Indeed, many previous studies have tried to model the bubble-induced turbulence based on this resemblance between BIT and SIT (Sato and Sekoguchi 1975; Theofanous and Sullivan 1982; Michiyoshi and Serizawa 1986).

3.4 Modeling of two-phase flow turbulence

As shown above, when $\langle \bar{\alpha} \rangle$ is small and the bubble–bubble interaction occurs little (cases 1 and 2), it is likely that the bubble-induced flow structure in the bubble wake would remain intact (Figs. 5, 6) and affect the bubble-induced turbulence. On the other hand, Liu et al. (2005) have measured that the Reynolds stress profile of the liquid flow induced by a chain of single bubble varies depending on the rising bubble path, i.e., straight, zigzag, and spiral ones. When bubbles rise in an oscillating path, which is the dominant motion in the present study, the Reynolds stress profile has an anti-symmetric shape with positive and negative peaks (Fig. 15a), whose magnitude increases with increasing the void fraction (i.e., bubble diameter and frequency). Thus, if we assume that such bubble-induced flow is retained at each radial position, as shown in Figs. 5 and 6, a superposition of them would show the contribution of bubble wake to the bubble-induced Reynolds stress. This idea can be tested by superposing a series of simplified Reynolds stress profile (Fig. 15a) whose peak values varies according to the local void fraction of interest, i.e., wall-peaking profile of the cases 1 and 2 (Fig. 7c). As shown in Fig. 15b, by superposing a radially distributed assumed Reynolds stress profile, it is possible to create a profile that qualitatively reproduces the Reynolds stress distributions of the cases 1 and 2; that is, it shows a 'double-S' shape that has larger main peaks near the wall and smaller secondary peaks at the core region. Due to wall-peaking condition, the gradient of local void fraction at the wall region is larger than that at the core region, which results in the larger

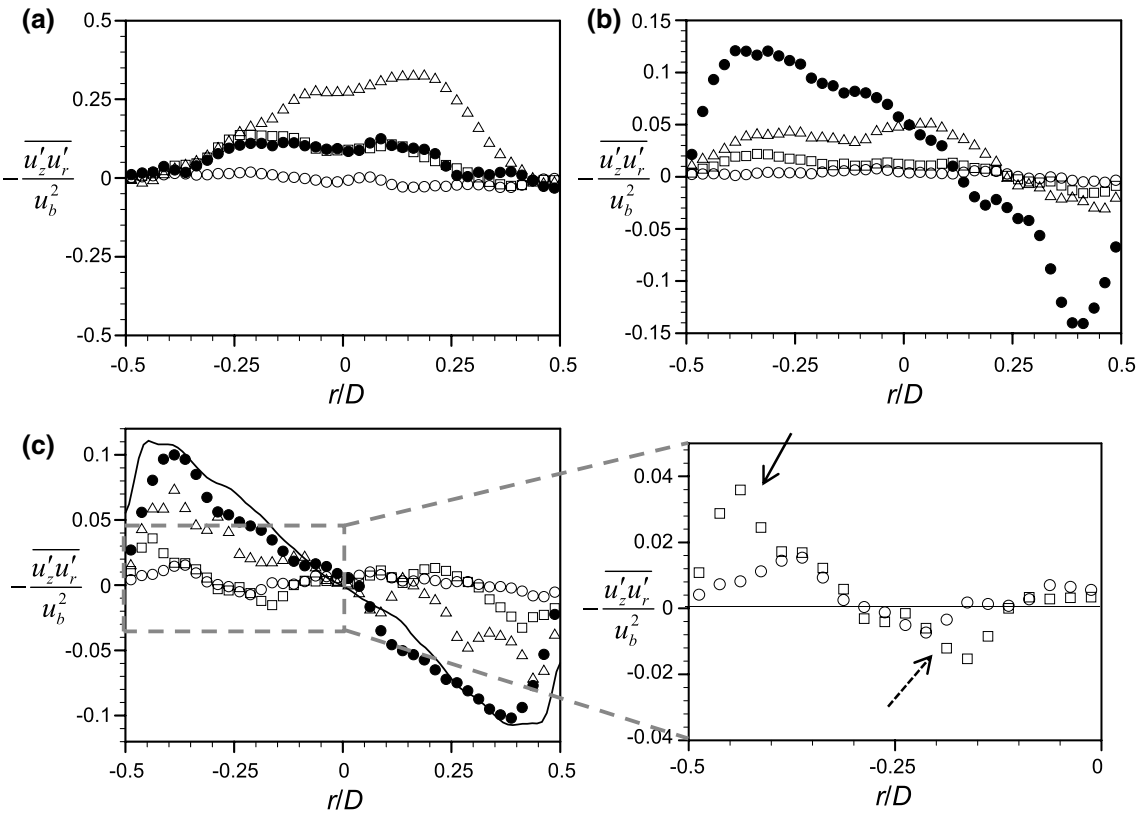

Fig. 14 Radial variations of Reynolds stress in liquid phase normalized by the bulk velocity (u_b) of single-phase flow, measured at $z/D = 4.5$ (**a**), 21 (**b**), and 42 (**c**). *Opened circle* case 1, *opened square* case 2, *opened triangle* case 3, *filled circle* case 4, *solid lines*, data for single-phase flow measured at $Re_D = 10^4$

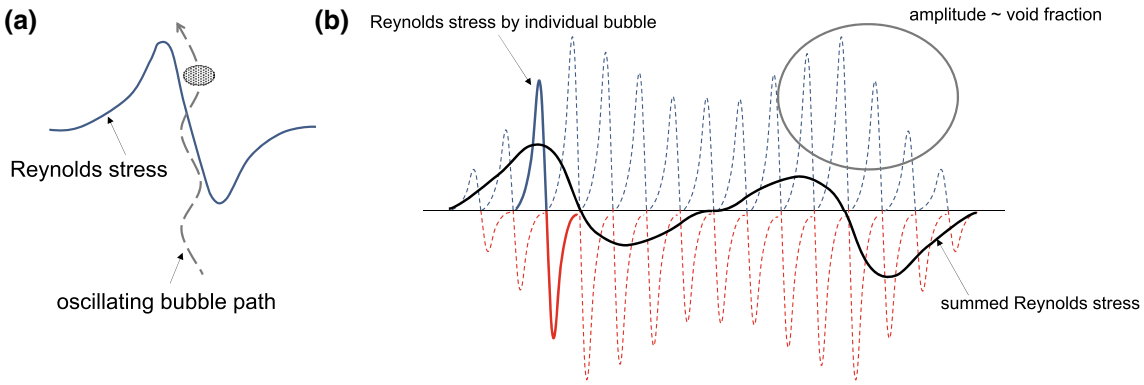

Fig. 15 **a** Sketch of the Reynolds stress profile induced by chain of rising bubbles in a *zigzag* or *spiral path*, adopted from the results of Liu et al. (2005). **b** Superposition of a series of modeled Reynolds stress profile corresponding to the wall-peaking condition

main Reynolds stress peaks near the wall than the secondary peaks. In addition, the sign of Reynolds stress profile changes where $\bar{\alpha}$ is maximum (Fig. 15b). In the present measurement, the same trend is observed for the cases 1 and 2. This is somehow obvious based on our concept such that the amplitude of Reynolds stress profile is largest at the void peak position. While several previous studies have reported that the position of void peak does not coincide with that of maximum Reynolds stress (Sato and Sekoguchi 1975; Michiyoshi and Serizawa 1986; Wang et al. 1987; Liu and Bankoff 1993; Shawkat et al. 2008), the reason for this difference has not been provided clearly. However, our analysis describes the distribution of bubble-induced Reynolds stress well in a qualitative manner. On the other

hand, for the cases 3 and 4 with a larger $\langle\bar{\alpha}\rangle$, the shape of Reynolds stress profile becomes different, indicating that other mechanism should be considered. As $\langle\bar{\alpha}\rangle$ increases, it is anticipated that interaction between bubbles occurs more frequently (Figs. 5, 6) and thus the resultant mean liquid velocity distribution will become gradually influential.

Now, let us mathematically model the bubble-induced Reynolds stress adopting the above idea. Starting from the well-known Sato's model based on the eddy viscosity assumption (Sato and Sekoguchi 1975), the shear stress (τ_b) by bubble-induced agitation is modeled as:

$$\tau_b = (1-\bar{\alpha})\rho_l \epsilon_b \frac{\partial \bar{u}_z}{\partial r}, \tag{6}$$

where ε_b is the eddy diffusivity. In the present study, the contribution from the individual bubble wake is considered in addition to the production of turbulence by the mean liquid velocity gradient. Thus, Eq. 6 is rewritten as:

$$\tau_b = (1-\bar{\alpha})\rho_l \left(\epsilon_b \frac{\partial \bar{u}_z}{\partial r} + \hat{\epsilon}_b \frac{\partial u_{si}}{\partial r}\right), \tag{7}$$

where u_{si} is the liquid velocity induced by individual bubble wake. The eddy diffusivity proposed by Sato and Sekoguchi (1975) is given by $\epsilon_b = c_1 \bar{\alpha}\langle \bar{d}_e\rangle\langle \bar{v}_r\rangle = c_1\bar{\alpha}\langle \bar{d}_e\rangle\langle \overline{u_{z,b}-u_z}\rangle$ (c_1 is a constant), which was derived based on the mixing length model. To find the expression for $\hat{\epsilon}_b$, we take the same approach as Sato and Sekoguchi (1975) and apply the fact that the bubble-induced flow velocity is confined close to the bubble surface (along the radial direction) (see Fig. 6a, b). As a result, we obtain

$$\hat{\epsilon}_b \sim \bar{\alpha}(r)\bar{d}_e(r)\bar{v}_r(r) = \bar{\alpha}(r)\bar{d}_e(r)\overline{u_{z,b}(r)-u_z(r)}. \tag{8}$$

Next, it is necessary to model u_{si}. From previous theoretical and experimental investigations (Batchelor 1967; Ellingsen and Risso 2001), it is known that u_{si} scales with the terminal velocity of a bubble (u_{bt}). On the other hand, as has been validated in Sect. 3.2, the scaling relation of $\langle\bar{v}_r\rangle \sim \langle\bar{\alpha}\rangle^{-0.1}$ is valid (Fig. 10b). Therefore, the following relation can be derived for u_{si}:

$$\bar{u}_{si} \sim \bar{u}_{bt} \sim \bar{v}_r(r)\bar{\alpha}(r)^{0.1}. \tag{9}$$

Substituting Eqs. 8 and 9 into Eq. 7, now the bubble-induced Reynolds stress is modeled as:

$$\tau_b = (1-\bar{\alpha})\rho_l \left[c_1\bar{\alpha}\langle\bar{d}_e\rangle\langle\bar{v}_r\rangle\frac{\partial\bar{u}_z}{\partial r} + c_2\left(\bar{d}_e\bar{v}_r\bar{\alpha}^{1.1}\frac{\partial\bar{v}_r}{\partial r} + 0.1\bar{d}_e\bar{v}_r^2\bar{\alpha}^{0.1}\frac{\partial\bar{\alpha}}{\partial r}\right)\right]. \tag{10}$$

It is noted that another constant c_2 is introduced for $\hat{\epsilon}_b$. In Eq. 10, thus the first term at the right-hand side explains the contribution from a time-averaged liquid velocity gradient and other two terms represent the contributions of the gradients of relative bubble velocity and void distribution, coming from the flow induced by individual bubble. Interestingly, Hosokawa and Tomiyama (2013), although they did not investigate the instantaneous flow structures including bubble dynamics, have proposed that the void fraction gradient is one of the sources of bubble-induced turbulence and corrected the Sato's model accordingly. Thus, their model has a similar form as ours, but the coefficients for each term are different. To apply the modeled turbulence to the experimental data, the process of tuning these coefficients according to the flow condition is necessary, which has been also tested by Hosokawa and Tomiyama (2013).

Figure 16 shows the comparison between the predicted and measured Reynolds stresses for the cases 1–4 (at $z/D = 42$). In each case, the tuned coefficients c_1 and c_2 to reduce the deviations using the least square error are shown as well. Except for the case 1, the suggested model predicts the bubble-induced turbulent stress fairly well; especially, the positions of main and secondary peaks are captured reasonably, as our model intended to achieve. Even for the case 1, the position of main peak is well captured. For now, it is not clear why the secondary peak deviates much from the measurement. Possibly, for this case with bubbles affecting the flow very intermittently, the flow statistics has not been developed fully enough, which needs to be investigated further. For the cases 2–4, it is noted that the coefficient c_2, which stands for the relative influence of flow structures induced by individual bubble, decreases as $\langle\bar{\alpha}\rangle$ increases. This agrees with what we have shown in previous sections. In the model by Hosokawa and Tomiyama (2013), which has not been further validated with actual experimental data, it is implied that the relative contributions of void fraction gradient and mean liquid velocity gradient remain the same even with different gas-phase conditions. As we have shown, however, it produces more reasonable and accurate predictions when we consider the relative dominance between these contributions. Since the idea of considering the contribution of void fraction and relative bubble rise velocity gradients to model bubble-induced turbulent stress is shown to provide reasonable predictions for laminar bubbly flows, it remains to be tested for turbulent flows for further refinement of the present model.

4 Concluding remarks

In the present study, empowered by the two-phase high-speed particle image velocimetry method, the spatial variations of both gas and liquid phases are measured simultaneously and analyzed in upward laminar bubbly pipe flows, while varying mean volume void fraction. While most previous studies focused on the statistically steady state

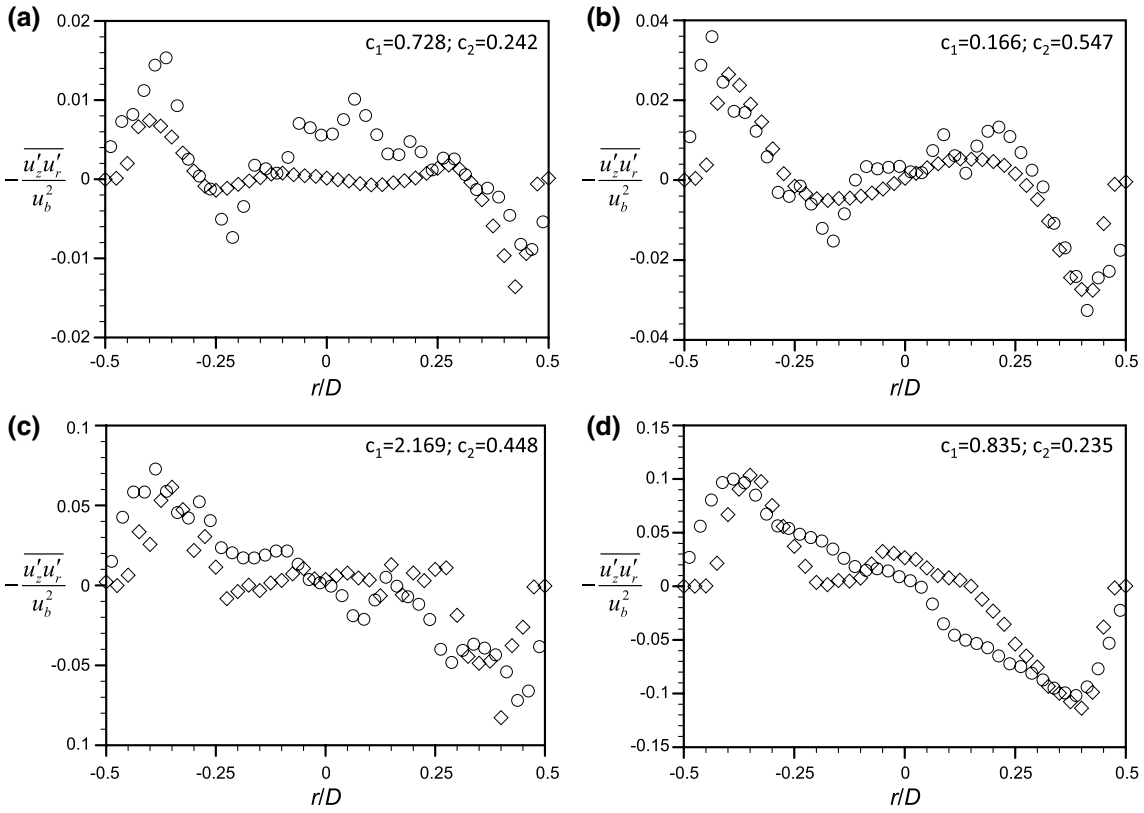

Fig. 16 Comparison between the modeled (*opened diamond*) and measured (*opened circle*) Reynolds stress distribution at $z/D = 42$: **a** case 1; **b** case 2; **c** case 3; **d** case 4

of gas–liquid flows (i.e., fully developed regime), here we have measured the evolution of the gas and liquid phases both at developing and at fully developed regions. As a result, due to mixing process, bubbles with an asymmetric initial distribution tend to migrate fast (following oscillating paths mostly) to show well-known wall- and intermediate-peaking conditions along the streamwise direction. Although the considered void fractions are not large, bubbles modulate the liquid-phase flow statistics significantly, of which effects saturate slower than the void distribution, as the flow develops. Mean liquid velocity shows a close relationship with local void distribution, and thus it is accelerated near the wall but decelerated (with a flat profile) at the core region, compared to that of single-phase laminar flow. Bubble-induced turbulence is enhanced significantly with increasing mean volume void fraction; it becomes comparable to that of a single-phase turbulent flow at moderate Reynolds numbers (e.g., 0.3–1 $\times$ 10^4 for the range of mean volume void fraction considered in the present study). Previously proposed scaling relations between two-phase flow statistics and mean void fractions are confirmed with our experimental data. On the other hand, the Reynolds stress profile shows an interesting trend with void fraction; that is, for smaller void fraction, it has a 'double-S' shape with main and secondary peaks, but changes to a 'single-S' shape similar to that of a typical single-phase turbulent flow for larger void fraction. Based on the measured bubble dynamics, we proposed a theoretical model for two-phase turbulent stress, which turned out to emphasize the contributions of non-uniform spatial distributions of local void fraction and relative bubble rise velocity in addition to that of mean liquid velocity gradient. The prediction with present model showed a good agreement with the measured experimental data. As a future research, we think that further refinement of the proposed model is necessary to make it applicable to turbulent bubbly flows.

Acknowledgments This work was supported by the National Research Foundation of Korea (NRF) Grant funded by the Korea government (MSIP) (NRF-2012M2A8A4055647, NRF-2013R1A1A1008373) via SNU-IAMD, and the Aspiring Researcher Program through Seoul National University (SNU) in 2014, Korea.

References

Adoua R, Legendre D, Magnaudet J (2009) Reversal of the lift force on an oblate bubble in a weakly viscous linear shear flow. J Fluid Mech 628:23–41

Adrian RJ, Westerweel J (2011) Particle image velocimetry. Cambridge University Press, New York

Antal SP, Lahey RT Jr, Flaherty JE (1991) Analysis of phase distribution in fully developed laminar bubbly two-phase flow. Int J Multiph Flow 17:635–652

Azitarte OE, Buscaglia GC (2003) Analytical and numerical evaluation of two-fluid model solutions for laminar fully developed bubbly two-phase flows. Chem Eng Sci 58:3765–3776

Baek SJ, Lee SJ (1996) A new two-frame particle tracking algorithm using match probability. Exp Fluids 22:23–32

Batchelor GK (1967) An introduction to fluid dynamics. Cambridge University Press, Cambridge

Biswas S, Esmaeeli A, Tryggvason G (2005) Comparison of results from DNS of bubbly flows with a two-fluid model for two-dimensional laminar flows. Int J Multiph Flow 31:1036–1048

Bröder D, Sommerfeld M (2007) Planar shadow image velocimetry for the analysis of the hydrodynamics in bubbly flows. Meas Sci Technol 18:2513–2528

Clift R, Grace JR, Weber ME (1978) Bubbles, drops, and particles. Academic Press Inc, London

Delnoij E, Kuipers JAM, Swaaij WPM, Westerweel J (2000) Measurement of gas-liquid two-phase flow in bubble columns using ensemble correlation PIV. Chem Eng Sci 55:3385–3395

Ellingsen K, Risso F (2001) On the rise of an ellipsoidal bubble in water: oscillatory paths and liquid-induced velocity. J Fluid Mech 440:235–268

Fujiwara A, Minato D, Hishida K (2004) Effect of bubble diameter on modification of turbulence in an upward pipe flow. Int J Heat Fluid Flow 25:481–488

Gonzalez RC, Woods RE, Eddins SL (2011) Digital image processing using MATLAB, 2nd edn. McGraw-Hill Education, Gatesmark

Gore RA, Crowe CT (1989) Effect of particle size on modulating turbulent intensity. Int J Multiph Flow 15:279–285

Hosokawa S, Tomiyama A (2004) Turbulence modification in gas–liquid and solid–liquid dispersed two-phase pipe flows. Int J Heat Fluid Flow 25:489–498

Hosokawa S, Tomiyama A (2013) Bubble-induced pseudo turbulence in laminar pipe flows. Int J Heat Fluid Flow 40:97–105

Ishii M, Zuber N (1979) Drag coefficient and relative velocity in bubbly, droplet or particulate flows. AIChE J 25:843–855

Jeong H, Park H (2015) Near-wall rising behaviour of a deformable bubble at high Reynolds number. J Fluid Mech 771:564–594

Kashinsky ON, Timkin LS, Cartellier A (1993) Experimental study of "laminar" bubbly flows in a vertical pipe. Exp Fluids 14:308–314

Kays WM, Crawford ME (1993) Convective heat and mass transfer, 3rd edn. McGraw-Hill Education, New York

Lance M, Bataille J (1991) Turbulence in the liquid phase of a uniform bubbly air-water flow. J Fluid Mech 222:95–118

Lau YM, Deen NG, Kuipers JAM (2013) Development of an image measurement technique for size distribution in dense bubbly flows. Chem Eng Sci 94:20–29

Lawson NJ, Rudman M, Guerra A, Liow J-L (1999) Experimental and numerical comparisons of the break-up of a large bubble. Exp Fluids 26:524–534

Lindken R, Merzkirch W (2002) A novel PIV technique for measurements in multiphase flows and its application to two-phase bubbly flows. Exp Fluids 33:814–825

Liu TJ, Bankoff SG (1993) Structure of air-water bubbly flow in a vertical pipe—I. Liquid mean velocity and turbulence measurements. Int J Heat Mass Transf 36:1049–1060

Liu Z, Zheng Y, Jia L, Zhang Q (2005) Study of bubble induced flow structure using PIV. Chem Eng Sci 60:3537–3552

Lu J, Biswas S, Tryggvason G (2006) A DNS study of laminar bubbly flows in a vertical channel. Int J Multiph Flow 32:643–660

Luo R, Pan XH, Yang XY (2003) Laminar light particle and liquid two-phase flows in a vertical pipe. Int J Multiph Flow 29:603–620

Martínez-Mercado J, Palacios-Morales CA, Zenit R (2007) Measurement of pseudoturbulence intensity in monodispersed bubbly liquids for $10 < Re < 500$. Phys Fluids 19:103302

Michiyoshi I, Serizawa A (1986) Turbulence in two-phase bubbly flow. Nucl Eng Des 95:253–267

Otsu N (1979) A threshold selection method from gray-level histograms. IEEE Trans Syst Man Cybern 9:62–66

Pang M, Wei J (2013) Experimental investigation on the turbulence channel flow laden with small bubbles by PIV. Chem Eng Sci 94:302–315

Rensen J, Luther S, Lohse D (2005) The effect of bubbles on developed turbulence. J Fluid Mech 538:153–187

Riboux G, Legendre D, Risso F (2013) A model of bubble-induced turbulence based on large-scale wake interactions. J Fluid Mech 719:362–387

Riboux G, Risso F, Legendre D (2010) Experimental characterization of the agitation generated by bubbles rising at high Reynolds number. J Fluid Mech 643:509–539

Risso F, Ellingsen K (2002) Velocity fluctuations in a homogeneous dilute dispersion of high-Reynolds-number rising bubbles. J Fluid Mech 453:395–410

Sathe MJ, Thaker IH, Strand TE, Joshi JB (2010) Advanced PIV/LIF and shadowgraphy system to visualize flow structure in two-phase bubbly flows. Chem Eng Sci 65:2431–2442

Sato Y, Sekoguchi K (1975) Liquid velocity distribution in two-phase bubble flow. Int J Multiph Flow 2:79–95

Serizawa A, Kataoka I, Michiyoshi I (1975) Turbulence structure of air-water bubbly flow—II. Local properties. Int J Multiph Flow 2:235–246

Shawkat ME, Ching CY, Shoukri M (2008) Bubble and liquid turbulence characteristics of bubbly flow in a large diameter vertical pipe. Int J Multiph Flow 34:767–785

So S, Morikita H, Takagi S, Matsumoto Y (2002) Laser Doppler velocimetry measurement of turbulent bubbly channel flow. Exp Fluids 33:135–142

Song Q, Luo R, Yang XY, Wang Z (2001) Phase distributions for upward laminar dilute bubbly flows with non-uniform bubble sizes in a vertical pipe. Int J Multiph Flow 27:379–390

Theofanous TG, Sullivan J (1982) Turbulence in two-phase dispersed flows. J Fluid Mech 116:343–362

Tryggvason G, Lu J (2015) Direct numerical simulations of bubbly flows. Mech Eng Rev 2:00220

Uno S, Kintner RC (1956) Effect of wall proximity on the rate of rise of single air bubbles in a quiescent liquid. AIChE J 2:420–425

Wang SK, Lee SJ, Jones OC Jr, Lahey RT Jr (1987) 3-D turbulence structure and phase distribution measurements in bubbly two-phase flows. Int J Multiph Flow 13:327–343

Westerweel J, Draad AA, van der Hoeven JGT, van Oord J (1996) Measurement of fully-developed turbulent pipe flow with digital particle image velocimetry. Exp Fluids 20:165–177

Zhou X, Doup B, Sun X (2013) Measurements of liquid-phase turbulence in gas-liquid two-phase flows using particle image velocimetry. Meas Sci Technol 24:125303